

UKAEA-CCFE-PR(25)352

Ivan Tolkachev, Felix Hofmann, Pui-Wai Ma

Simulations of Nanocrystalline Iron Formation under High Shear Strain

Enquiries about copyright and reproduction should in the first instance be addressed to the UKAEA Publications Officer, Culham Science Centre, Building K1/O/83 Abingdon, Oxfordshire, OX14 3DB, UK. The United Kingdom Atomic Energy Authority is the copyright holder.

The contents of this document and all other UKAEA Preprints, Reports and Conference Papers are available to view online free at scientific-publications.ukaea.uk/

Simulations of Nanocrystalline Iron Formation under High Shear Strain

Ivan Tolkachev, Felix Hofmann, Pui-Wai Ma

Simulations of Nanocrystalline Iron Formation under High Shear Strain

Ivan Tolkachev* and Felix Hofmann†

Department of Engineering Science, University of Oxford, United Kingdom

Pui-Wai Ma‡

*United Kingdom Atomic Energy Authority, Culham Science Centre,
Abingdon, Oxfordshire, OX14 3DB, United Kingdom*

High-shear methods have long been used in experiments to refine grain structures in metals, yet the underlying mechanisms remain elusive. We demonstrate a refinement process using molecular dynamic simulations, wherein nanocrystalline structures are generated from initially perfect lattices under high-shear strain. The simulation cells undergo a highly disordered state, followed by recrystallization and grain coarsening, resulting in nanograins. We explore the dependence on parameters such as temperature, heat dissipation rate, shear strain rate, and carbon impurity concentration. Higher temperatures lead to the formation of larger and longer grains. The faster heat dissipation sample initially yields more small grains, but their number subsequently reduces, and is lower than the slower heat dissipation sample at approximately 1.5 strain. Slower strain rates do not promote nanograin formation. The presence of carbon impurities appears to have little effect on grain formation. This detailed analysis affords insight into the mechanisms that control the formation of nanograins under high-shear conditions.

I. INTRODUCTION

Grain refinement can be achieved through various methods, including the use of chemical refiners or spray-forming techniques [1]. An attractive approach to accomplish grain refinement is through severe plastic deformation (SPD) techniques, such as accumulative roll bonding (ARB) and equal channel angular pressing (ECAP) [2]. High-shear methods, such as high-pressure torsion (HPT), can significantly alter the microstructure of metals. Numerous materials, including Al, Cu, and Mg alloys, have shown a reduction in grain size with increasing shear strain [3–7]. Yusuf *et al.* [7] observed a reduction in grain size with increasing shear strain for 316L stainless steel, which also correlates with an increase in Vickers microhardness. Despite numerous experimental studies attempting to elucidate the mechanisms of nanocrystalline formation with increased shear strain, the results are inconclusive. [8].

The leading theory for grain refinement suggests that dislocations are generated in the material due to shear strain. These dislocations accumulate and form subgrain boundaries. As the shear strain increases, dislocations are annihilated at these boundaries, leading to a rise in the misorientation angle between the grains. Some of the formed dislocations are not absorbed and persist, forming low-angle grain boundaries (LAGBs), which perpetuates the grain refinement process [4, 8–10].

Other factors can also influence grain refinement, such as the number and distribution of precipitates within the material [11–13], as well as the presence of twinning deformation [14, 15]. Isik *et al.* [16] observed a

significant contribution to grain subdivision and induced grain refinement through a deformation-induced martensitic phase transformation, from $\gamma \rightarrow \epsilon$ phase in Co-28Cr-6Mo alloy.

Numerous computational methods have been employed to explore the mechanism of grain refinement through plastic shearing. Finite element analysis (FEA) has been used to understand how the HPT process can modify the samples [17–20]. FEA simulations greatly depend on the constitutive model used during the simulation [21]. As such, the physics of a given FEA system are largely defined by the constitutive model which may not allow other physical mechanisms of grain refinement to exist within the simulation, which in turn affects the observable deformation modes. Nevertheless, numerous FEA studies have been conducted that draw conclusions on possible grain refinement mechanisms under shear strain. Wei *et al.* [22] investigated the mechanisms of grain refinement in single crystal Ni subjected to HPT, employing crystal plasticity finite element simulations. The results proposed the existence of two rotation modes that directly contributed to the formation of grain boundaries with high misorientations. Additionally, FEA simulations of high angle pressing (HAP) were conducted by Frydrych *et al.* [23] to explore the mechanism of grain refinement in an already nanocrystalline face-centered cubic (FCC) material. This study confirmed that grain orientation was a major indicator of their susceptibility to further refinement. The study calculated the Taylor factor, which is a function of lattice orientation, for grains in the original configurations. The study showed that grains which had larger Taylor factors were more prone to refinement. A larger Taylor factor correlates to greater plastic work done, when compared over the same range of slip [24]. The work of Frydrych [23] makes no further attempt to quantify the orientations making it difficult to obtain exact lattice orientations which were more prone

* Ivan.Tolkachev@eng.ox.ac.uk

† Felix.Hofmann@eng.ox.ac.uk

‡ Leo.Ma@ukaea.uk

to refinement.

Molecular dynamics (MD) simulations have been employed to study microstructural evolution in metals subjected to SPD [25–31]. However, most of these studies start with simulation cells that are already in a nanocrystalline state, and therefore, do not explore the mechanisms by which a single crystal can transform into a nanocrystalline state. Interestingly, the work of Nikonov [31] used MD simulations to shear a perfect, single crystal simulation cell. However, the results were only used for shear stress vs. strain comparisons with a polycrystalline box, and no conclusions were reached about the single crystal shear. The work of Guan *et al.* [32] attempted to replicate the HPT process using an MD simulation of Aluminum. However, similar to the other MD investigations mentioned above, the initial box was already in a nanocrystalline state before the shearing took place, and thus, there was no investigation into the actual formation of nanocrystals.

The precise underlying processes responsible for the development of a nanocrystalline microstructure via HPT remains elusive. Despite the significant disparity between shear rates in simulations and experimental settings, we conducted molecular dynamics simulations on iron to gain insights into potential mechanisms through which shear could induce the formation of nanocrystalline structures. Additionally, we scrutinized the progression of microstructures to facilitate meaningful comparisons with experimental outcomes.

Iron is chosen as the material of the current study because of its diverse uses in domestic and industrial applications. Especially, in advanced fission and future fusion reactors [33–35], iron-based steels, such as ferritic/martensitic (FM) steels, are chosen as the structural material. FM steels have the same body-centred cubic (BCC) crystal structure as iron. It was shown experimentally that FM steels exhibited less neutron irradiation-induced swelling than austenitic steels with face-centred cubic (FCC) structure [36].

In the following, we first discuss our simulation methods. Then, we present our simulation results and discuss potential mechanisms underlying the observed phenomena. We also draw comparisons with experimental HPT studies.

II. SIMULATION SETUP

All MD simulations were carried out using LAMMPS [37]. Simulation cells were created using Atomsk [38]. We constructed perfect crystal simulation cells with $80 \times 80 \times 80$ unit cells, where each unit cell contains 2 atoms in BCC structure with a lattice parameter of 2.8665 \AA , corresponding to Fe. Each simulation cell contains 1,024,000 atoms. The starting crystal orientations are $x = [100]$, $y = [010]$, and $z = [001]$. Periodic boundary conditions are applied in all three directions.

We also examined the effect of carbon impurities. We

created simulation cells by adding 102 carbon atoms into those perfect cells at random positions. This corresponds to a carbon impurity content of 100 appm.

We adopted the interatomic potential for Fe developed by Ackland *et al.* [39], which has been widely used to investigate the microstructure evolution of iron [40–43]. For Fe-C simulations, we used the Hepburn-Ackland FeC interatomic potential [44], which was developed based on the aforementioned Ackland Fe potential. It has been used in several studies concerned with the effect of carbon on the microstructural evolution of iron [45–48].

The trajectory of a system of interacting atoms is governed by the Langevin equation of motion:

$$\frac{d\mathbf{r}_i}{dt} = \mathbf{v}_i \quad (1)$$

$$m \frac{d\mathbf{v}_i}{dt} = \mathbf{F}_i - \gamma \mathbf{v}_i + \mathbf{f}_i \quad (2)$$

where \mathbf{r}_i , \mathbf{v}_i , and $\mathbf{F}_i = -\partial U / \partial \mathbf{r}_i$ are position, velocity, and force associated with atom i . U is the interatomic potential energy. m is the mass of an atom. The temperature is controlled by the Langevin thermostat, where the damping parameter γ is related to the delta-correlated fluctuating force \mathbf{f}_i according to the fluctuation-dissipation theorem [49, 50], namely,

$$\langle \mathbf{f}_i(t) \rangle = 0, \quad (3)$$

$$\langle f_{i\alpha}(t) f_{j\beta}(t') \rangle = \mu \delta_{ij} \delta_{\alpha\beta} \delta(t - t'), \quad (4)$$

where α and β are Cartesian coordinates, and

$$\mu = 2\gamma k_B T. \quad (5)$$

The fluctuation and dissipation of atoms can be considered as a result of electron-phonon interaction, so γ describes the strength of electron-phonon coupling. We used the electron-phonon coupling parameter for Fe according to Mason *et al.* [51], such that $\gamma = 6.875 \text{ eV fs \AA}^{-2}$. We denote this as γ_1 . In some simulations, we used a damping parameter that is ten times larger, which is denoted as $\gamma_2 = 10\gamma_1$. If we do not explicitly mention the value of γ below, we are using γ_1 .

Before applying any shear, the simulation cells are thermalised to particular temperatures. The cell volumes are also relaxed isotropically, so they attain stress-free conditions.

Shear was imposed by continually deforming the simulation cell. The shear strain is applied on the xy plane with displacement in the x direction. This was done by imposing a cell tilt factor change, which is effectively an engineering strain. A total simulation time of 335 ps was used, with a maximum final shear strain of $\varepsilon = 10$. This means the shear rate $d\varepsilon/dt$ is approximately $2.985 \times 10^{10} \text{ s}^{-1}$. We also performed the same simulation with a 10 times longer simulation time, corresponding to a 10 times lower strain rate.

To avoid boundary self-interactions, we can remap the simulation cell when the tilting is more than 0.5 of the

cell length. The cell vector and the positions of atoms are remapped along the shearing direction, with the simulation cell going from a 0.5 to a -0.5 tilt. It is important to note that, due to the periodic boundary conditions, there is no change in the local atomic environment.

We used OVITO [52] for analysis. Grains are identified using the grain segmentation modifier. The minimum grain size was chosen as 50 atoms. We discuss the effect of using a different number of atoms as the minimum grain size in Appendix A3. Since this algorithm requires the crystal orientation of each atom, the polyhedral template matching (PTM) modifier [53] is adopted beforehand. PTM can determine the local crystal orientation of each atom in terms of a quaternion, where each quaternion can be projected into Rodrigues space [54]. Then, the orientation of each atom in this space can be visualised by mapping orientation to an RGB colouring scheme [55]. Dislocation lines are detected using the dislocation analysis (DXA) modifier [56].

III. RESULTS

We first present the results of our simulations exploring the influence of shear strain on initially perfect, single crystalline iron. Next, we investigate the behaviour of samples under various conditions, including differing temperatures, damping parameters, strain rates, and the presence of carbon impurities.

A. Shear-induced nanocrystalline structure

Figure 1 shows a key result of this work. Figure 1a to 1g show the simulation cell at different shear strains. The results reveal a process in which nanograins are formed due to shear strain in a real-space representation. This simulation was run for 335 ps, up to $\varepsilon = 10$, at a constant strain rate, at a temperature of 300 K, and with a constant damping parameter of γ_1 . We will refer to this as the *benchmark* simulation. The colouring of each atom in Figure 1 is based on its crystal orientation. Only atoms detected as BCC structures are shown. Since a similar colour means a similar crystal orientation, one can clearly observe the formation of nanograins in real space. We are not aware of any similar simulations showing the formation of nanograins under high shear strains in the literature.

Figure 1a shows the initially perfect crystal simulation cell. It is subjected to a shear strain in the xy direction, which causes the atoms to gradually lose their BCC structure. At around 0.27 strain, there is a high level of atomic disorder, as shown in Figure 1b. Most atoms deviate from the BCC structure. We can consider that atoms are now in a disordered state. Shortly after that, a recrystallization process begins, as shown in Figure 1c, at around 0.3 strain. Many small grains are visible. Between Figure 1c and 1d, grain formation clearly occurs,

with the atomic crystal orientations still largely similar. By Figure 1e, at 4 strain, the atomic crystal orientations are largely dissimilar, with grains exhibiting different orientations. It appears that the grain refinement process continues between 4 and 7 strains, see Figure 1f. Then, the grain number and sizes attain a dynamical quasi-steady state.

Grain growth has been observed for different metals in simulations [32, 57] and experiments [58]. These investigations typically focus on samples that already possess a grain structure before applying any strain or stress. A fundamental difference is that the current simulations start with a perfect crystal structure. Our results show that when shear strain is applied, atoms become highly disordered, followed by recrystallisation into a polycrystalline structure. However, such a mechanism does not always occur in different simulation conditions, as will be discussed below.

For a more detailed analysis, we can consider Figure 2 alongside Figure 1. Figure 2a shows the average atomic potential and kinetic energy as a function of shear strain. Figure 2b is an enlarged version that only covers a range of up to 1 shear strain. When the shear strain is first applied, there is a gradual increase in the potential energy up to a value of around -3.73 eV/atom. The initial potential energy increment appears parabolic, suggesting a linear elastic response, as the elastic potential energy is proportional to ε^2 . The maximum point of potential energy occurs at 0.27 strain, which is the point shown in Figure 1b. The disordered state is a state of high potential energy.

Then, the potential energy in the system gradually reduces to around -3.89 eV/atom and remains roughly at this value for the remaining shearing process. At 0.27 strain, where the potential energy reaches its peak, we also observe a rapid increase in the kinetic energy of the system, as shown in Figure 2b, from a value of 0.039 eV/atom to 0.072 eV/atom, peaking at 0.3 strain. This increase is followed by a sharp decrease, reaching a value of around 0.042 eV/atom, at which the simulation plateaus for the continued shearing. Since the estimated system temperature is directly proportional to the kinetic energy, we observe a substantial increase in temperature at 0.27 strain, as shown in Figure 2c. The maximum temperature reaches 560 K, which is far below 1,811 K, the melting temperature of iron.

Figure 2d illustrates the number of grains detected by OVITO. The number of grains undergoes a sharp increase at 0.25 strain and peaks at 0.27 strain with approximately 400 grains. This corresponds to the highly disordered state, where OVITO identifies small pockets of BCC structure as individual grains within a volume of highly disordered atoms. After that, there is a rapid decrease in grain number, reaching a minimum of 25 grains at around 0.3 strain, coinciding with the decrease in potential energy. Following this, the number of grains once again rises to around 230 at 2 strains. Then, there is a decrease to about 160 at 3 strains. Another increase in

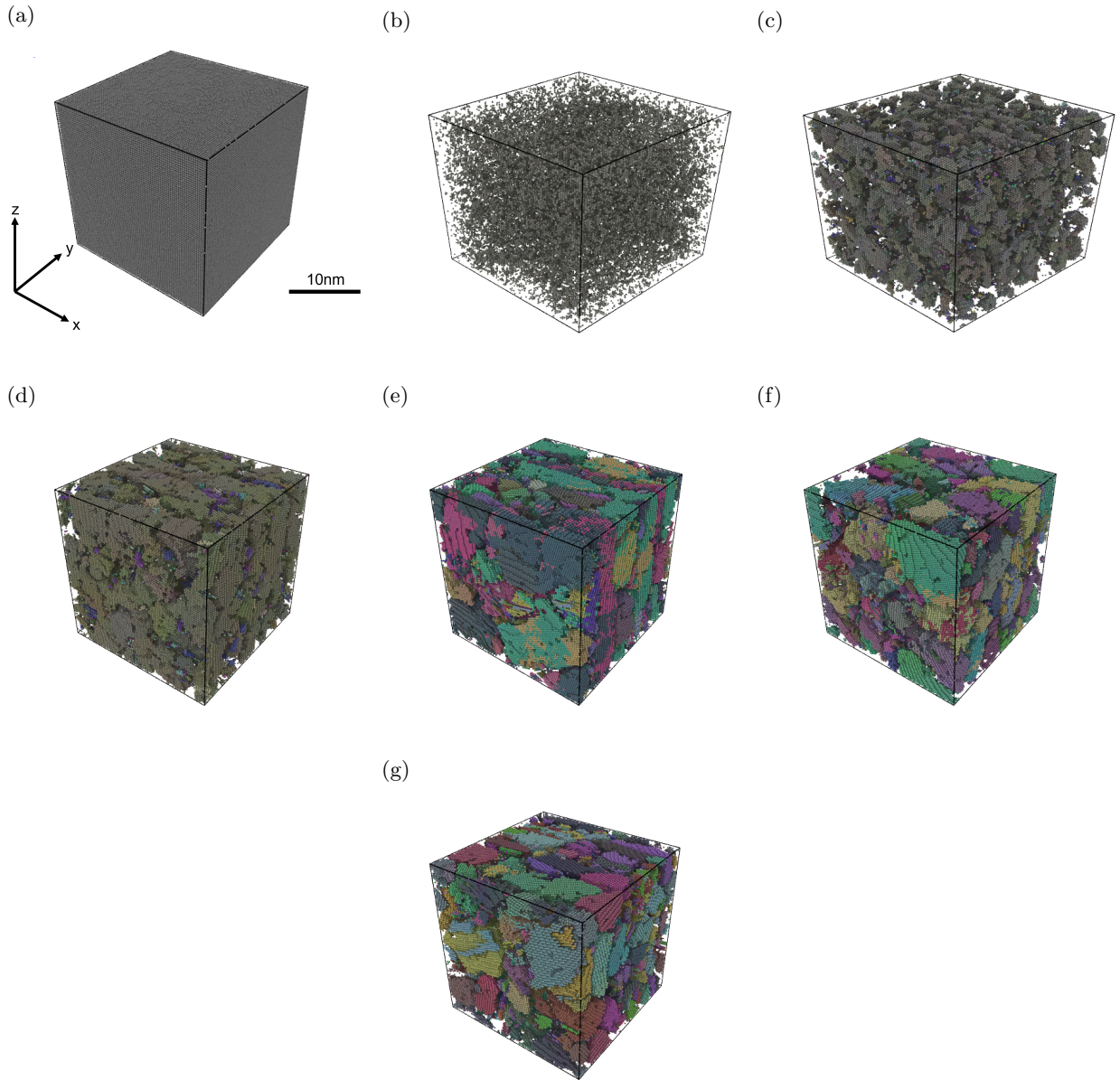


FIG. 1: Grain refinement process with atoms coloured by crystal orientations. Temperature $T = 300$ K. Strain rate $d\varepsilon/dt = 1/33.5 \text{ ps}^{-1} \approx 2.985 \times 10^{10} \text{ s}^{-1}$ and damping parameter $\gamma = 6.875 \text{ eV fs } \text{\AA}^2$. (a) 0 Strain (b) Highly Disordered - 0.27 Strain (c) Recrystallisation - 0.32 Strain (d) 1 Strain (e) 4 Strains (f) 7 Strains (g) 10 Strains.

grain count is observed after reaching 6 strains, plateauing at a value of around 240 until the end of the simulation. In Figure 2e, we also observe an increase in dislocation density starting at a strain value of 0.27. The dislocation density is given as the total line length divided by the volume of the simulation cell. Dislocation density rises to approximately $2.6 \times 10^{-3}/\text{\AA}^2$ at 0.82 strain, followed by a decrease to $1.2 \times 10^{-3}/\text{\AA}^2$ at around 2 strain. The dislocation density experiences a slight increase to $1.6 \times 10^{-3}/\text{\AA}^2$ at 3 strains and subsequently remains relatively constant during further shearing.

The average atomic von Mises stress, as shown in Fig-

ure 2f, and the potential energy per atom are well correlated. There is an initial increase in von Mises stress, followed by a rapid decrease when the highly disordered state is formed at 0.27 strain. Nikonov [31] also found an increase in stress during the single crystal shearing of BCC iron. The same rapid increase, followed by a sharp decrease, was observed and attributed to lattice reorientation. It is noteworthy that the potential energy never decreases to its original value, as some excess energy, associated with dislocations and grain boundaries generated during deformation, is stored within the material [59].

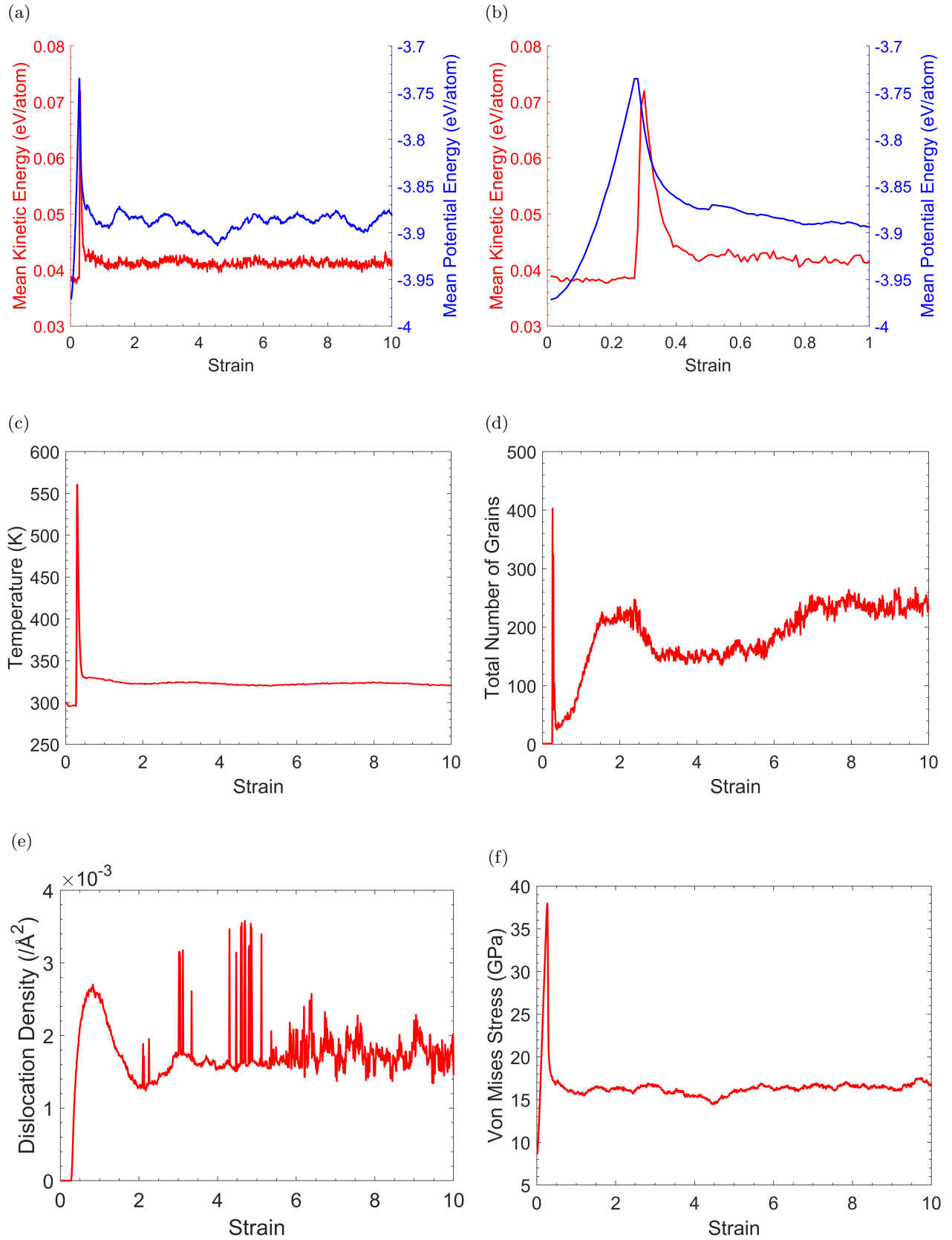


FIG. 2: Benchmark simulation data plotted as a function strain. Temperature . Strain rate $d\varepsilon/dt = 1/33.5 \text{ ps}^{-1} \approx 2.985 \times 10^{10} \text{ s}^{-1}$ and damping parameter $\gamma = 6.875 \text{ eV fs } \text{\AA}^2$. (a) Kinetic and Potential Energy (b) Kinetic and Potential Energy up to 2 strains (c) Temperature (d) Number of Grains (e) Dislocation Density (f) von Mises Stress

As shown in Figure 1, the atoms become highly disordered up to 0.27 strain, which corresponds to a maximum in the potential energy. This maximum is a threshold value after which the atoms within the lattice move and reorganise themselves, as made evident by the increase in kinetic energy in Figure 2b, and the recrystallisation at 0.3 strain in Figure 1c. This increasing shear strain causes a break of the symmetry in the crystal lattice that changes the potential energy landscape. Since atoms already have a high potential energy, triggered by thermal excitations, the unbalanced forces acting on atoms cause them to accelerate, triggering the onset of the disordered phase.

Subsequently, there is a surge in system temperature, as shown in Figure 2c, which is due to the increase in atomic velocities. As our system is attached to a Langevin thermostat, the system temperature reduces back to the target temperature. Alongside the cool-down, the system undergoes a recrystallization, causing grain nucleation. The grains are tiny at around 0.3 strain, see Figure 1c. The microstructure remains dominated by highly disoriented regions. Then, grain coarsening starts and continues, as observed in Figure 2d. This can be driven by the excess free energy of the disordered region manifesting as grain boundaries, as grain boundaries are known to possess excess free energy [60]. This excess free energy provides the driving force for atomic transport and subsequent grain growth [61].

In Fig 2e, the dislocation density in the simulation cell increases and peaks at around 0.82 strain. Dislocations also possess excess free energy [60], which may also contribute to grain growth. We note an important point regarding the DXA: LAGBs can be recognised as arrays of dislocations. Therefore, it is unclear if the detected dislocations are grain boundaries or dislocations within grains. There is a new approach that may resolve this situation. Ma *et al.* [62] suggested a new algorithm to calculate the shortest distance of any atom from the determined grain boundaries. By eliminating atoms close to the grain boundaries, one can estimate the dislocation line density inside grains. However, we have not adopted this method in our current work, because the definition of grains is somewhat ambiguous in such a highly disordered structure. Additional analysis on this is provided in Appendix A2.

Experimental studies have exhibited similar trends for nanocrystalline formation. Studies on Fe-8% Al [63], TiAl [64], AZ91 Mg [65], and NiTi [66], all used some form of hot deformation to induce strain into the material, followed by quenching. These studies observed small, recrystallised grains compared to the original structure.

Figure 3 shows the atomic crystal orientation, total energy, von Mises stress, and dislocation lines at different shear strain values. The total energy is the sum of atomic potential and kinetic energy. The figure keys for the total energy and von Mises stress are shown in Figure 3a. In the DXA analysis, green lines represent dislocations with

Burgers vector $\mathbf{b} = \frac{1}{2}\langle 111 \rangle$, and pink lines represent $\mathbf{b} = \langle 100 \rangle$. Figure 3 shows that most dislocation lines have $\mathbf{b} = \frac{1}{2}\langle 111 \rangle$. Only few dislocations have $\mathbf{b} = \langle 100 \rangle$. This agrees with the experimental findings in the literature on iron, iron-chromium alloys and ferritic/martensitic steels [67–69].

Next, we consider the total energy and von Mises stress, see Figure 3. Initially, the atoms within the box have low energy and low stress. As the atoms become disordered, they experience a high energy and stress state, as shown by the colouring in Fig. 3c. As recrystallisation occurs, it is evident that some atoms return to the low energy and stress state, whilst others remain in the high energy and stress state (Fig. 3d). As shear strain is continually applied, we can observe areas of both high and low energy and stress. The areas of low energy and low stress correspond to atoms within the grains and are BCC in nature, whilst the areas of high energy and high stress correspond to atoms which are not BCC in nature, and are not shown in the crystal orientation images. As such, Figure 3 shows that the atoms between the grains have high energy and high stress, which confirms the presence of grain boundaries in the simulation box [60].

B. Temperature

To further probe the underlying mechanisms for nanocrystalline formation from perfect crystal under high-shear strain, certain simulation variables were altered one by one. We first changed the thermostat temperature, whilst keeping all other conditions unchanged. Three additional simulations were carried out with thermostat temperatures $T = 500$ K, 800 K, and 1000 K. Figure 4 shows the kinetic energy, the potential energy, the temperature, the number of grains, the dislocation density, and the von Mises stress of different simulations.

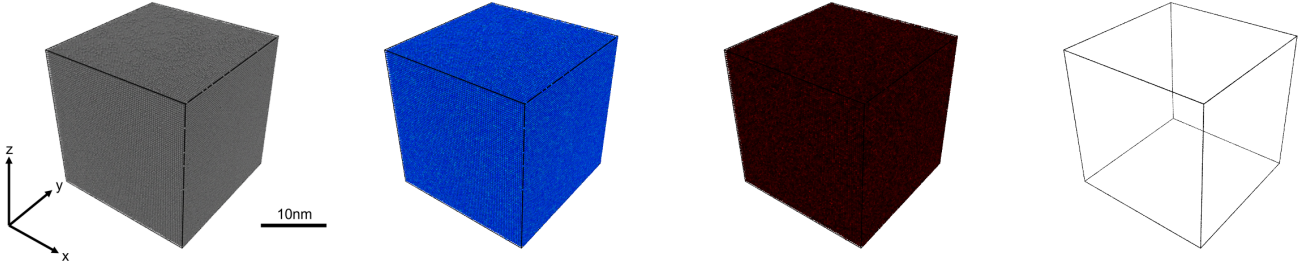
Figure 4a and 4b show the change in kinetic energy. They are well correlated with the system temperature in Figure 4e because of the linear dependence between temperature and kinetic energy. We observe a notable difference in the increase in kinetic energy associated with the formation of the disordered phase at different thermostat temperatures. For example, the kinetic energy increases from around 0.039 eV/atom to 0.072 eV/atom for the 300 K simulation, having an increase of 0.033 eV/atom, whilst the 800 K simulation experiences a spike from 0.1 eV/atom to around 0.117 eV/atom, which is an increase of 0.017 eV/atom, much less than the increment at 300 K. We can also observe from Figure 4b that the initial increase in kinetic energy occurs earlier for the higher temperature simulations, occurring at 0.27 strain for the 300 K, 0.25 strain for the 500 K, 0.2 strain for the 800 K, and 0.19 strain for the 1000 K simulations.

The increase in kinetic energy corresponds to a decrease in potential energy. Figure 4c and 4d show how the potential energies begin to decrease earlier for the higher temperature simulations. Interestingly, the ther-

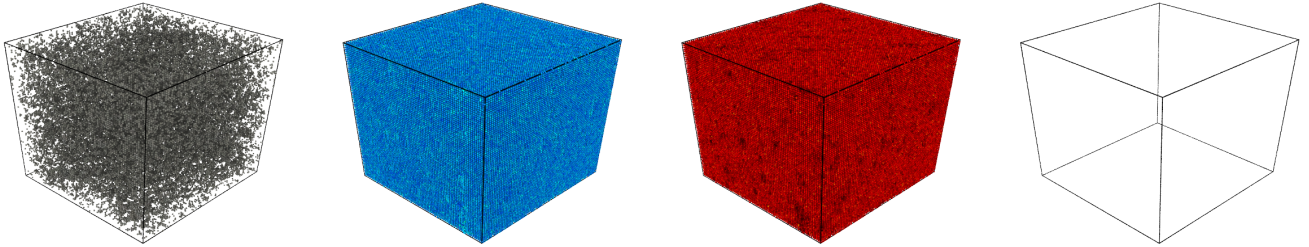
(a) Key; Total Energy Left; von Mises Stress Right



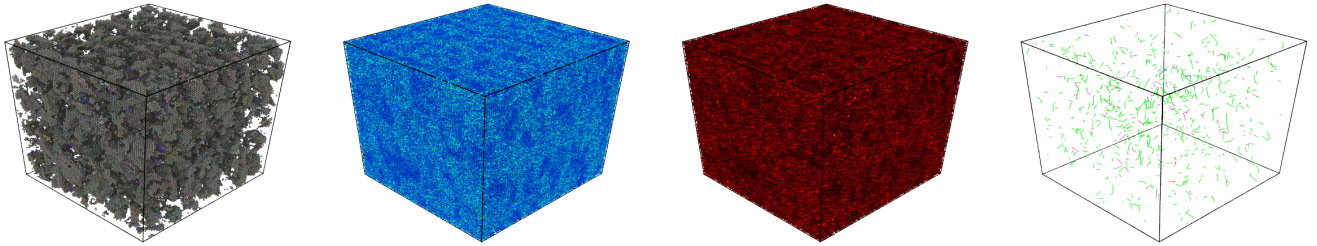
(b) 0 Strain - Benchmark



(c) Disordered Phase - 0.27 Strain - Benchmark



(d) Recrystallisation - 0.32 Strain - Benchmark



(e) 1 Strain - Benchmark

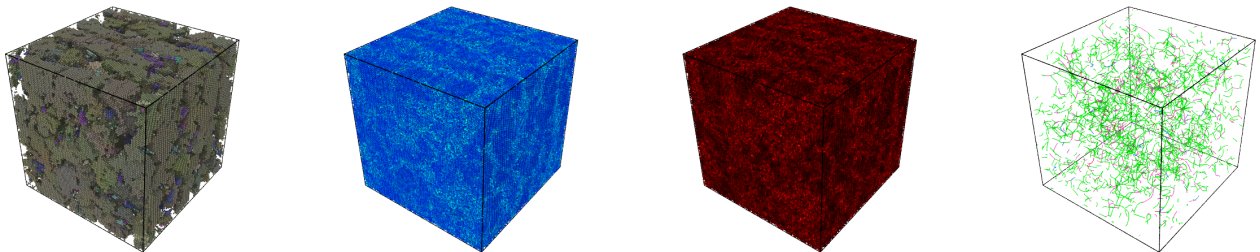
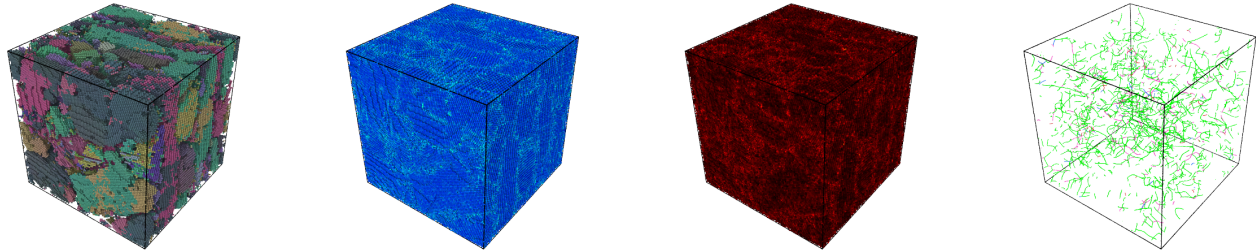
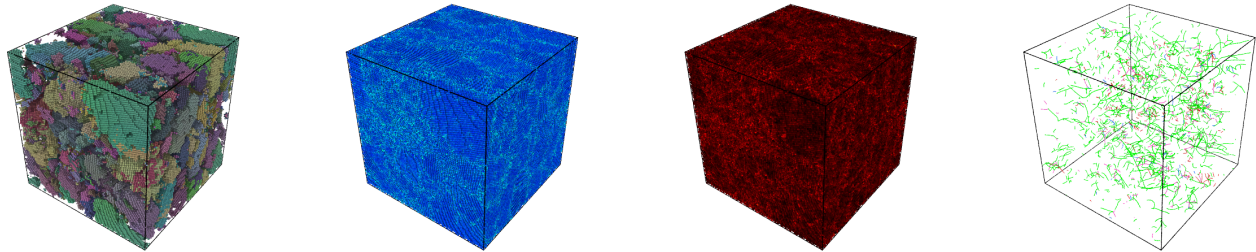


FIG. 3: Benchmark simulation visualisations. Strain rate $d\varepsilon/dt = 1/33.5 \text{ ps}^{-1} \approx 2.985 \times 10^{10} \text{ s}^{-1}$ and damping parameter $\gamma = 6.875 \text{ eV fs } \text{\AA}^2$. Colour key found in (a). Left - Atoms coloured by crystal orientations; Centre-left - Total energy; Centre-right - von Mises stress; Right - Dislocation analysis; for different levels of strain in benchmark simulation.

(f) 4 Strain - Benchmark



(g) 7 Strain - Benchmark



(h) 10 Strain - Benchmark

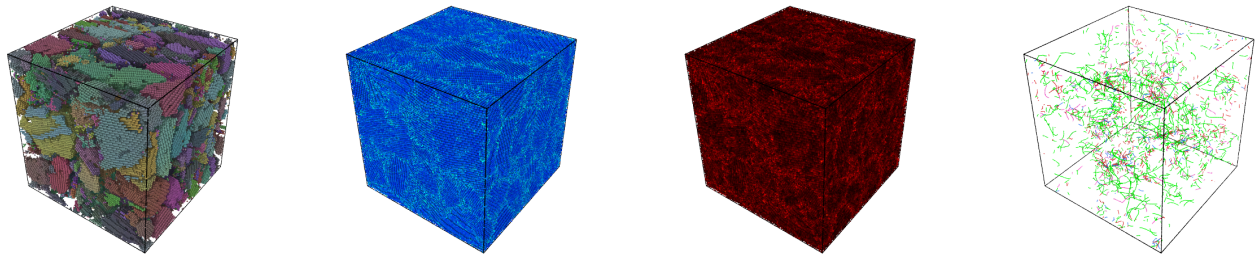


FIG. 3: Benchmark simulation visualisations. Strain rate $d\varepsilon/dt = 1/33.5 \text{ ps}^{-1} \approx 2.985 \times 10^{10} \text{ s}^{-1}$ and damping parameter $\gamma = 6.875 \text{ eV fs } \text{\AA}^2$. Colour key found in (a). Left - Atoms coloured by crystal orientations; Centre-left - Total energy; Centre-right - von Mises stress; Right - Dislocation analysis; for different levels of strain in benchmark simulation.

mostat temperature does not appear to significantly alter the maximum potential energy. Whilst the 300 K simulation increases to a maximum of -3.73 eV/atom , the higher temperature 500 K and 800 K simulations increase to -3.74 eV/atom , and the 1000 K simulation increases to -3.72 eV/atom . The higher temperature simulations generally experience higher potential energy after the initial spike, with the 1000 K simulation hovering at around -3.82 eV/atom after 4 strains, whilst the 300 K simulation plateaus at around -3.89 eV/atom .

Inspection of Figure 4f and 4g provides interesting insight into the effect of the thermostat temperature change. All simulations experience an initial spike in grain number, with the spike occurring at a lower strain for higher temperature simulations. The magnitude of

the increase does not appear to correlate with thermostat temperature. For example, whilst the 300 K simulation increases to around 400 grains, the 1000 K simulation only increases to around 195 grains, which is less than the 500 K simulation, but more than the 800 K simulation.

All simulations show a rapid decrease in grain number between 0.19 and 0.25 strain, followed by an increase in grain number strain ~ 2 strains. The 300 K simulation notably has the most grains at the local maximum point of 2 strains. The other temperature simulations have fewer grains at this point, with the 500 K, 800 K, and 1000 K simulations having roughly the same number of grains up to 4 strains. The grain number in the 500 K and 800 K simulations increases and saturates after 7

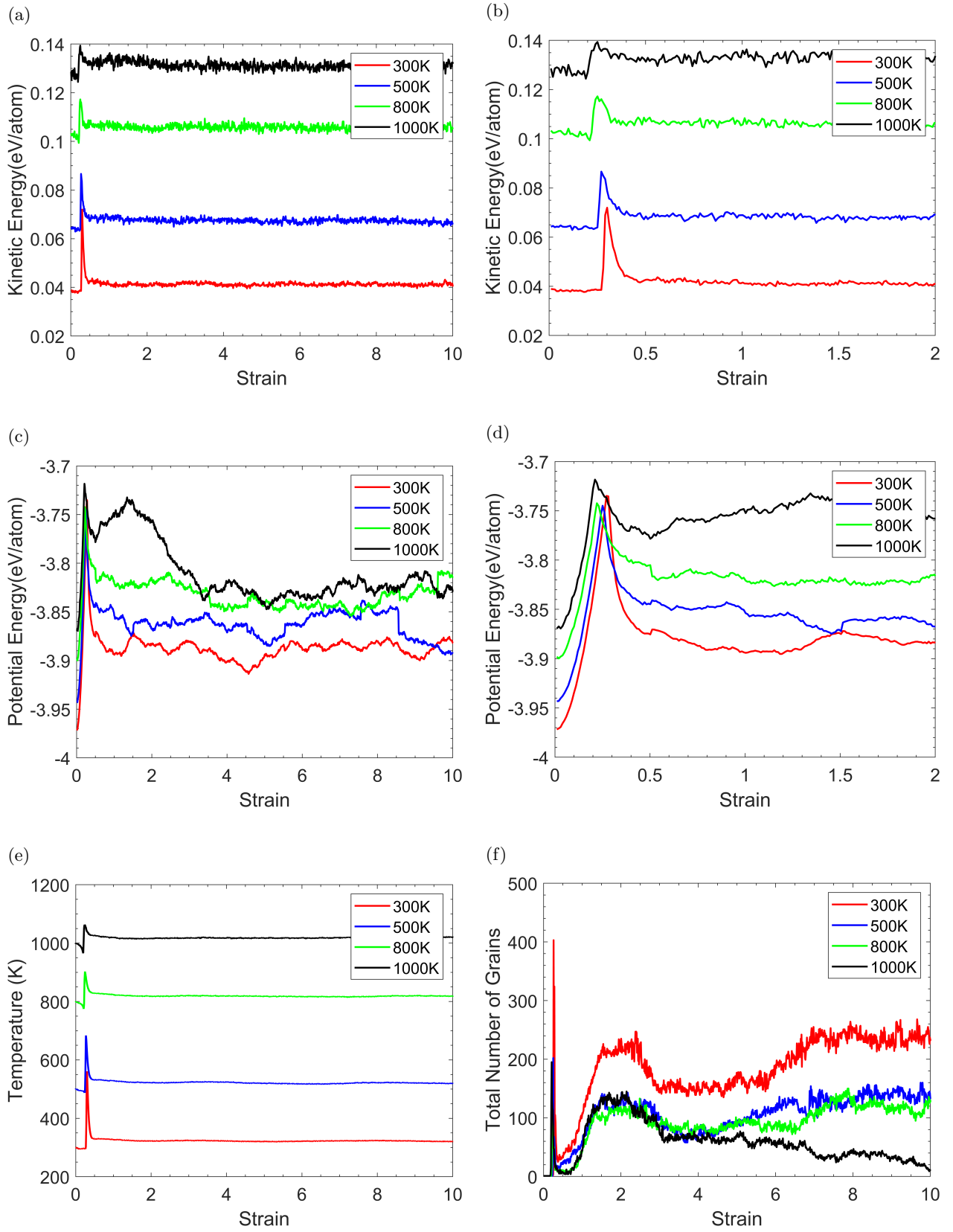


FIG. 4: Simulation data plotted as a function of strain at different thermostat temperatures. Strain rate $d\varepsilon/dt = 1/33.5 \text{ ps}^{-1} \approx 2.985 \times 10^{10} \text{ s}^{-1}$ and damping parameter $\gamma = 6.875 \text{ eV fs } \text{\AA}^2$. Red line - 300 K, Blue line - 500 K, Green line - 800 K, Black line - 1000 K. (a) Kinetic Energy (b) Kinetic Energy up to 2 strains (c) Potential Energy (d) Potential Energy up to 2 strains (e) Temperature (f) Number of Grains (g) Number of Grain up to 2 strains (h) Von Mises Stress up to 2 Strains (i) Dislocation Density.

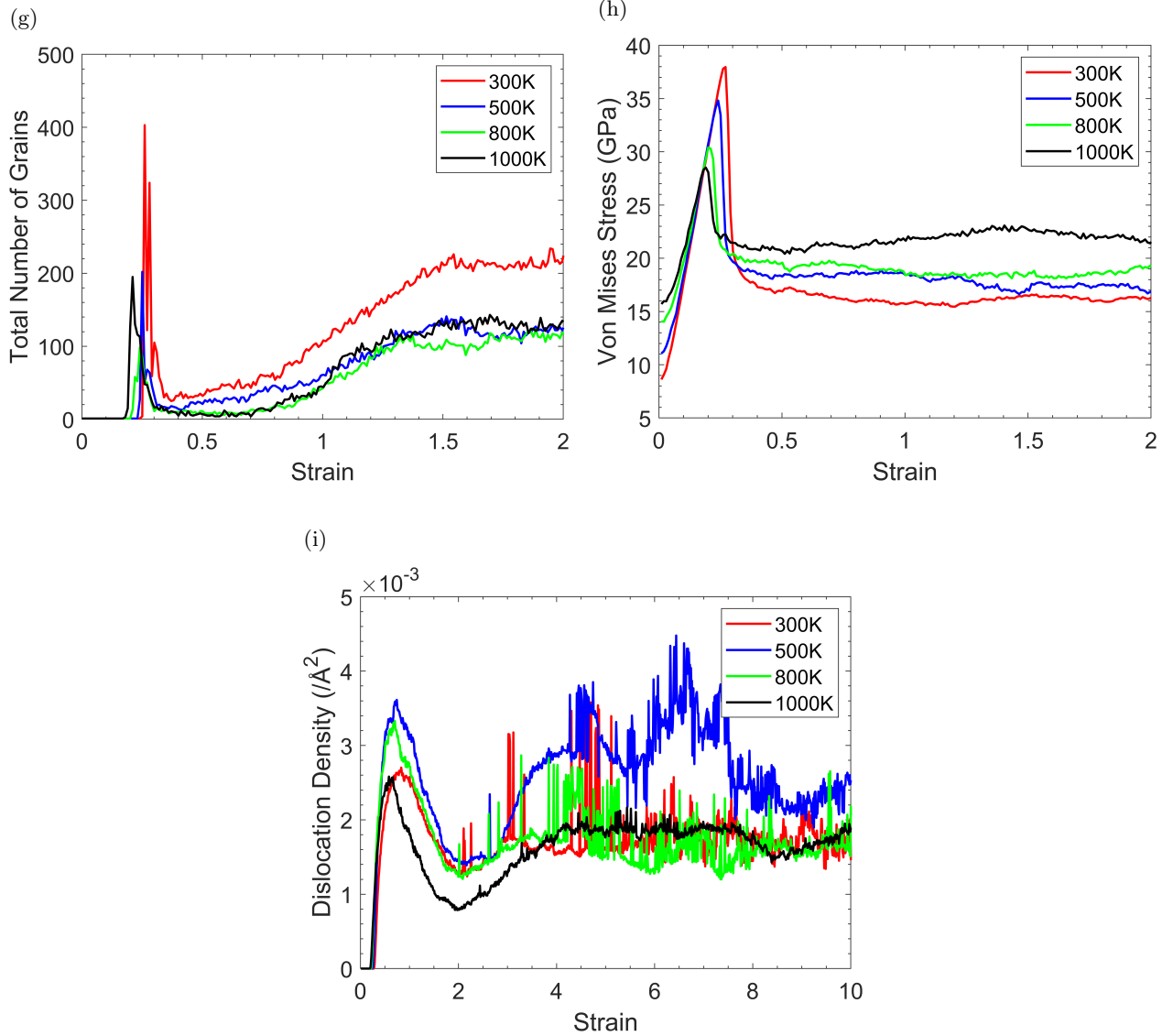


FIG. 4: Simulation data plotted as a function of strain at different temperature simulations. Strain rate $d\varepsilon/dt = 1/33.5 \text{ ps}^{-1} \approx 2.985 \times 10^{10} \text{ s}^{-1}$ and damping parameter $\gamma = 6.875 \text{ eV fs \AA}^2$. Red line - 300 K, Blue line - 500 K, Green line - 800 K, Black line - 1000 K. (a) Kinetic Energy (b) Kinetic Energy up to 2 strains (c) Potential Energy (d) Potential Energy up to 2 strains (e) Temperature (f) Number of Grains (g) Number of Grain up to 2 strains (h) Von Mises Stress up to 2 Strains (i) Dislocation Density.

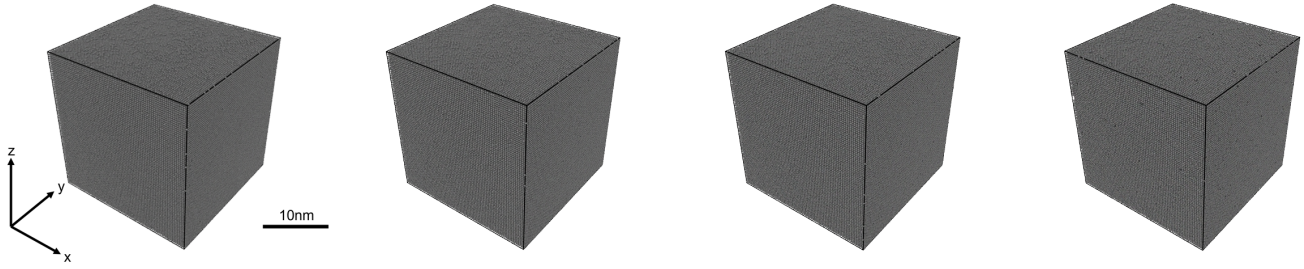
strains. The 1000 K simulation experiences a reduction in grain number after 4 strains, and is as low as 11 grains at 10 strains.

Figure 4h shows the von Mises stress. The stress directly correlates with the potential energy. This is evident in the figure as the decrease in stress after the initial increase occurs at exactly the same strain value as the potential energy decrease (see Figure 4c and 4d). Nevertheless, whilst the potential energy maximum is roughly the same value for all simulations, the von Mises stress experiences an unequal increase. As made evident by Figure 4h, the higher temperature simulations show a

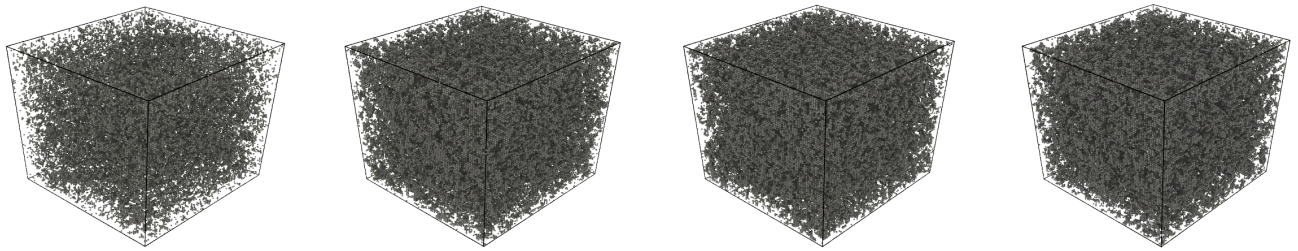
lower maximum von Mises stress and as the simulation temperature decreases, the maximum von Mises stress increases. The subsequent decrease in von Mises stress is also larger in magnitude for the lower temperature simulations, and the value at which the stress plateaus with shearing is lower for the lower temperature simulations.

We observe in Figure 4i that the dislocation densities for the higher temperature simulations also follow the same pattern as the benchmark simulation. For each simulation, there is a marked increase in dislocation density at the exact strain value where the kinetic energy begins to increase, and the potential energy decreases. This is

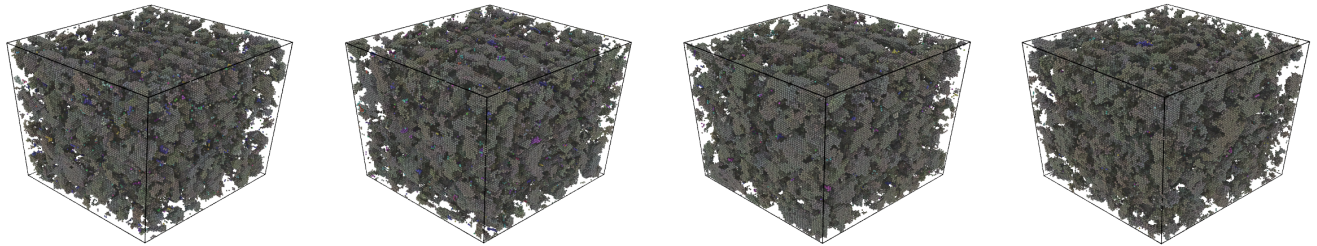
(a) 0 Strain



(b) Disordered Phase



(c) Recrystallisation



(d) 1 Strain

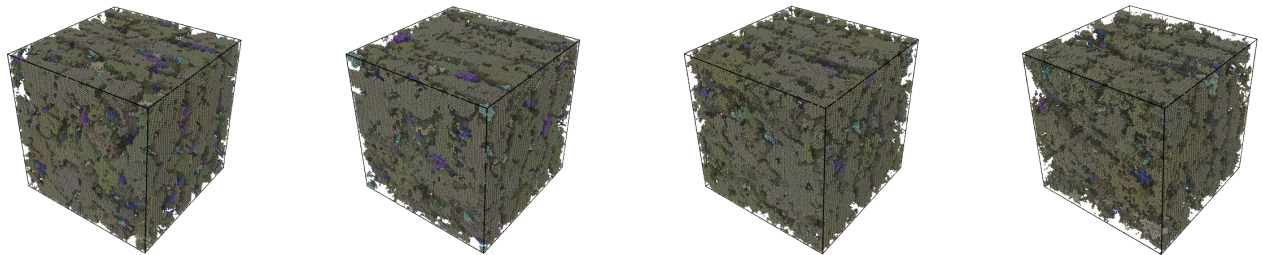
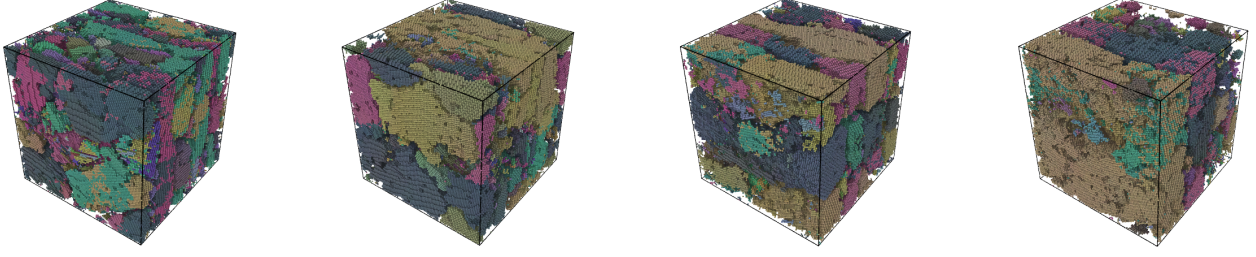
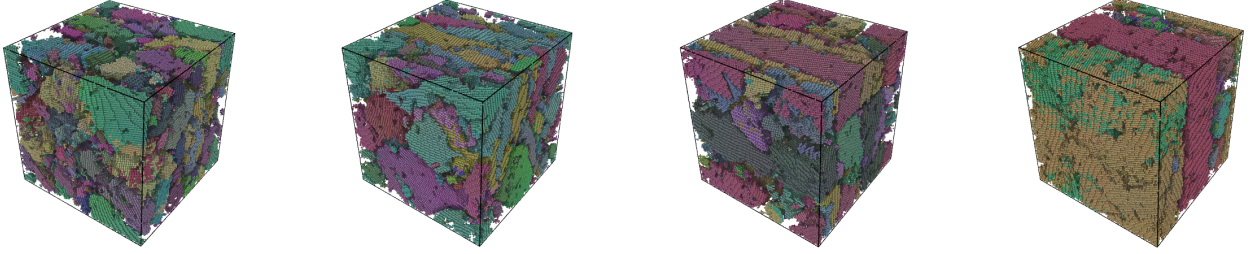


FIG. 5: Atoms coloured by orientation for different temperature simulations. Strain rate $d\varepsilon/dt = 1/33.5$ $\text{ps}^{-1} \approx 2.985 \times 10^{10} \text{ s}^{-1}$ and damping parameter $\gamma = 6.875 \text{ eV fs } \text{\AA}^2$. Left - T = 300 K Simulation; Centre-left - T = 500 K Simulation; Centre-right - T = 800 K Simulation; Right - T = 1000 K Simulation.

(e) 4 Strains



(f) 7 Strains



(g) 10 Strains

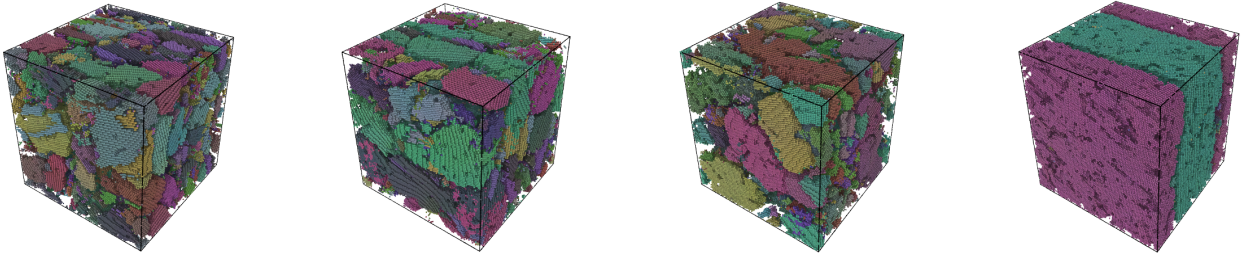


FIG. 5: Atoms coloured by orientation for different temperature simulations. Strain rate $d\varepsilon/dt = 1/33.5 \text{ ps}^{-1} \approx 2.985 \times 10^{10} \text{ s}^{-1}$ and damping parameter $\gamma = 6.875 \text{ eV fs } \text{\AA}^2$. Left - $T = 300 \text{ K}$ Simulation; Centre-left - $T = 500 \text{ K}$ Simulation; Centre-right - $T = 800 \text{ K}$ Simulation; Right - $T = 1000 \text{ K}$ Simulation.

followed by a maximum point in dislocation density, occurring at 0.82 strain for the 300 K simulation, 0.74 strain for the 500 K simulation, 0.7 strain for the 800 K simulation, and 0.6 strain for the 1000 K simulation. We note that the maximum value of dislocation density does not correlate with temperature. Both the 500 K and 800 K simulations have larger dislocation densities, whilst the 300 K and 1000 K simulations have lower maximum densities. As with the benchmark simulation, the dislocation densities decrease up to 2 strains, after which there is another increase and saturation in dislocation density for all simulations.

In Figure 4d, there appears to be a nearly universal maximum potential energy, around -3.73 eV/atom , for every simulation. This value corresponds to the maximum potential energy the material can sustain before

atoms are permanently displaced from their lattice positions, and is the value attained before the initiation of the disordered atomic state. After this point, the potential energy decreases while the kinetic energy increases. The higher temperature simulations exhibit higher potential energy at 0 strain due to the principle of equipartition of energy. At higher temperatures, a system under strain should reach the point of instability, in terms of potential energy, more easily. This, in turn, causes the kinetic energy to increase at an earlier strain value, and the higher temperature simulations experience the initiation of the disordered state at a lower strain. This observation could explain the discrepancy in the von Mises stress peak among the varying simulations. The stress applied to reach a certain potential energy is reduced because the potential energy is already at a higher level. Similarly,

this also explains why the spike in grain number occurs earlier for the higher temperature simulations.

Interestingly, upon analyzing Figure 4f and 4i, we observe that the peak in grain number after recrystallization (at 2 strains) directly corresponds to a minimum value in dislocation density after the disordered phase. This finding aligns with previous MD simulations of nanocrystalline Cu [25]. The study found that at high dislocation density, a system is highly unstable when nanocrystalline grains are present. With applied strain, the dislocations were able to glide towards and annihilate at grain boundaries.

To further understand the effect of temperature on nanograin production, we can observe Figure 5. This figure depicts the local atom orientations based on their colouring, and once again only atoms in the BCC phase are visualized. The simulations, from left to right are at 300 K, 500 K, 800 K, and 1000 K, respectively. All simulations begin with a perfect box, thermalised to the desired temperature (Figure 5a). With applied shear strain, the cells all enter a highly disordered state (Figure 5b). The level of disorderness appears to be larger for the lower temperature simulations. This is shown visually in that the number of BCC atoms is less for the 300 K simulation compared to, for example, the 1000 K simulation.

Each simulation experiences a subsequent recrystallization (Figure 5c), followed by a grain growth up to 1 strain (Figure 5d). At this point, through inspecting the colouring of atoms, the majority of atoms have similar crystal orientations, leading to a proposition that the misorientation between grains is not large. As the shearing continues, it is evident that grains are in different orientations, as shown in Figure 5e - 5g. It is also evident that the grains are larger and longer for the higher temperature simulations compared to the lower temperature simulations. This is observed by comparing the 300 K and 1000 K simulations in Figure 5g, whereby the grain number and size are very different between simulations. This is the reason why the grain numbers for the higher temperature simulations are lower compared to the 300 K benchmark, as depicted in Figure 4f.

As α -iron is a BCC metal, it has a very high stacking fault energy [70]. It is generally agreed that Dynamic Recovery (DRV) is the sole dynamic restoration mechanism in α -iron and other ferritic metals [70, 71]. However, some studies have also shown that Dynamic Recrystallisation (DRX) occurs in BCC iron [31, 72]. Typically, DRV readily occurs in ferritic steels and iron at temperatures $> 0.4T_m$ [73]. On the other hand, the data presented in Figure 4i suggests that this can also occur at room temperature, and there is a marked annihilation of dislocations present within the figure. The fundamental mechanisms of DRV are dislocation glide, climb, and cross-slip [70]. We speculate that the accumulation of dislocations also contributes to nanocrystalline formation as the dislocations accumulate and form LAGBs. In general, the dislocation densities stay fairly constant after around 4 strains for all simulations, whilst

the grains continue to elongate, which is especially common for higher temperature simulations. This behaviour is expected from a metallic material under constant strain deformation [70, 74].

C. Heat dissipation

The heat dissipation from the lattice subsystem to the environment is represented by the Langevin thermostat. In metals, the dominant heat transfer mechanism is through electrons [75]. Therefore, we take the damping parameter γ , which governs the speed of heat dissipation, according to the phonon-electron coupling. The damping parameter has, so far, been kept at $\gamma = 6.875 \text{ eV fs } \text{\AA}^{-2} = \gamma_1$. To investigate the effect of the speed of heat dissipation on the nanocrystalline formation due to shear strain, a further simulation was carried out with a damping parameter of $\gamma = 68.75 \text{ eV fs } \text{\AA}^{-2} = \gamma_2$. All other conditions were kept the same. The Langevin thermostat was set to 300 K.

Figure 6 shows various properties as a function of shear strain when two different damping parameters are used. We also compare the percentage of BCC structure found in the simulation cell as a function of strain. This will become important when considering Figure 7, which compares the evolution of the atom orientation in simulations using different damping parameters.

Figure 6a shows the change in kinetic energy between the lower (or benchmark) and higher damping simulations. The average kinetic energy, in the lower damping simulation, increases from around 0.038 eV/atom to 0.072 eV/atom, a difference of 0.034 eV/atom, before reducing to a dynamically quasi-steady state. Similarly, the higher damping simulation experiences an increase from 0.034 eV/atom to around 0.045 eV/atom, a difference of 0.011 eV/atom, before it drops. The magnitude and difference of the increase are much lower for the higher damping simulation because a higher damping parameter leads to a higher quenching rate. The kinetic energy is also noticeably lower for the higher damping simulation as both simulations reduce to a dynamically quasi-steady state. The lower damping simulation plateaus at 0.042 eV/atom whilst the higher damping simulation sits at 0.039 eV/atom.

Figure 6b shows that both simulations experience an identical increase in potential energy with an increase of shear strain up to a value of -3.73 eV/atom at 0.27 strain, corresponding to the highly disorder state. However, whilst the benchmark simulation reduces to and hovers around -3.89 eV/atom, the higher damping simulation only decreases to around -3.82 eV/atom, which suggests that it is in a higher state of disorder. Furthermore, the potential energy experiences a gradual decrease after around 4 strains, until it is roughly at the same value as the benchmark simulation at 10 strains. As before, the average atomic von Mises stress, as shown in Figure 6d, and the potential energy per atom, are well

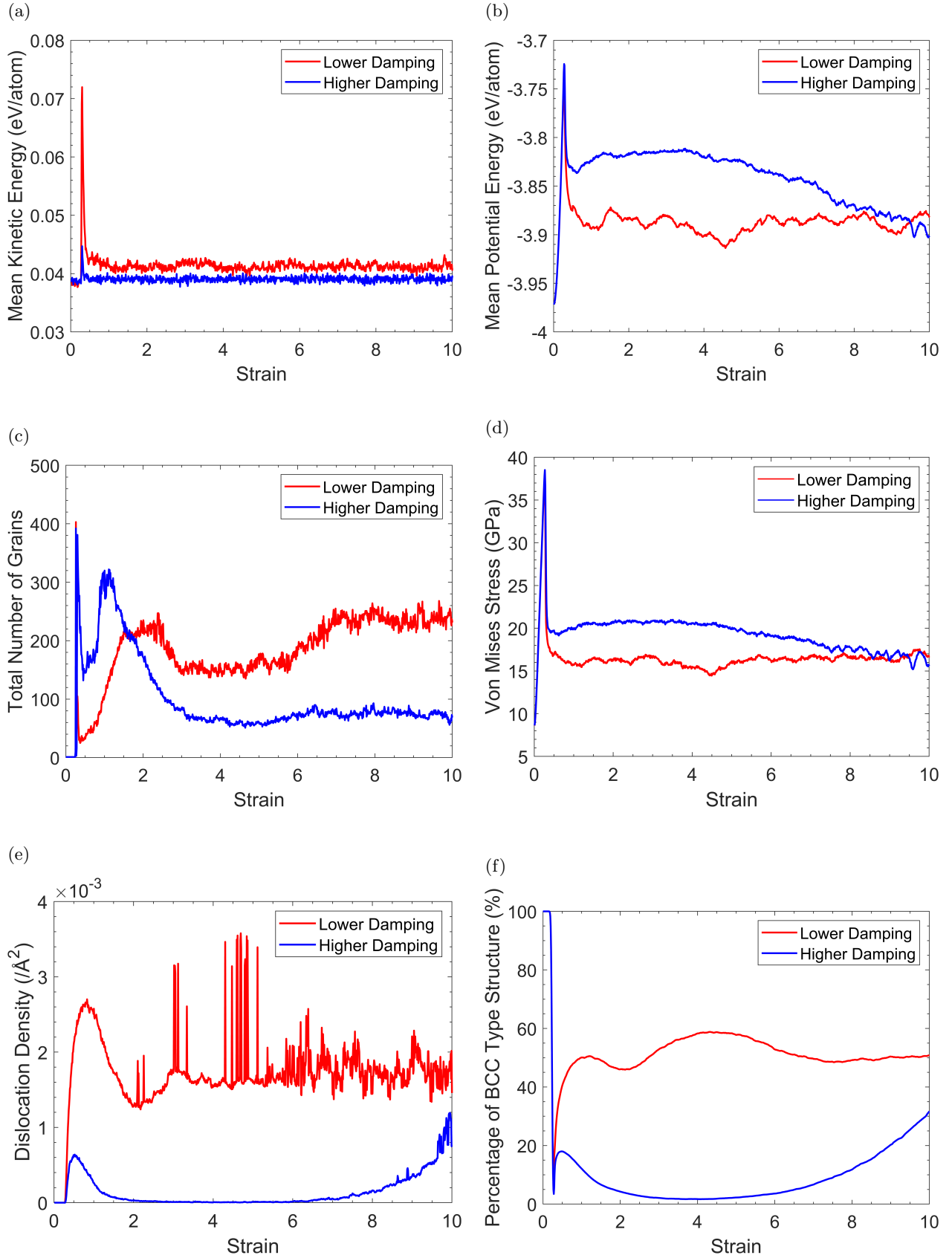


FIG. 6: Simulation data plotted as a function of strain using different damping parameters. Strain rate $d\varepsilon/dt = 1/33.5 \text{ ps}^{-1} \approx 2.985 \times 10^{10} \text{ s}^{-1}$. Damping parameter $\gamma = 6.875 \text{ eV fs } \text{\AA}^2$ for Red line and damping parameter $\gamma = 68.75 \text{ eV fs } \text{\AA}^2$ for Blue line. (a) Kinetic Energy (b) Potential Energy (c) Number of Grains (d) von Mises stress (e) Dislocation Density (f) Percentage of BCC Structure.

correlated for both simulations.

Next, we consider the grain counts in the simulation cells in Figure 6c. Both the benchmark and higher damping simulations exhibit significant disordered states at 0.27 strain. The benchmark cell contains about 400 grains, while the higher damping simulation shows 390. Both simulations show a rapid decrease in grain count. The benchmark simulation subsequently drops to around 30 grains, whereas the higher damping simulation only drops to around 130 grains. The benchmark simulation steadily increases in grain count until about 2 strains, reaching approximately 220 grains. In contrast, the higher damping simulation rapidly rises to 320 grains around 1.1 strain, then sharply declines. By 3 strains, the higher damping simulation maintains around 70 grains, plateauing until the end of simulation, a lower count than the benchmark simulation's plateau at 240 grains.

By observing Figure 6e, which shows the dislocation densities for the simulations, we see the initial spike in dislocation density is much lower for the higher damping simulation. Whilst the benchmark simulation increases to around $2.6 \times 10^{-3}/\text{\AA}^2$ at 0.82 strain, the higher damping simulation's dislocation density only increases to $6.4 \times 10^{-4}/\text{\AA}^2$ at 0.51 strain. With increased shearing, the dislocation density for the benchmark simulation decreases and then saturates at around $1.6 \times 10^{-3}/\text{\AA}^2$. This is contrary to the data obtained for the higher damping simulation whereby the dislocation density decreases to 0 at around 2 strains and begins to increase at around 6.5 strains, with the dislocation density for the higher damping simulation peaking at around $1.2 \times 10^{-3}/\text{\AA}^2$ at 10 strains.

Figure 6f shows the percentage of the overall structure in the BCC phase as a function of strain. We show that both simulations experience a highly disordered state transition at 0.27 strain, where the percentage of BCC atoms within the cells are below 10% for both simulations. However, the benchmark simulation experiences a rapid recovery of the BCC phase, and around 50% of the atoms within the simulation cell are considered to be BCC after 1 strain. Conversely, the higher damping simulation makes a slight recovery to 17% at 0.44 strain, before reducing to 2% BCC. After 5 strains, the higher damping cell begins to recover its BCC structure. This increases to around 32% BCC at 10 strains.

To further understand the data presented in Figure 6, a visual representation of atomic crystal orientation is shown in Figure 7. Both simulations begin with a perfect cell (Figure 7a) before experiencing a disordered state (Figure 7b) followed by a recrystallisation (Figure 7c). The number of atoms in the disordered phase is much larger for the higher damping simulation. During the recrystallisation, the grains appear to be much larger for the benchmark simulation, with many small pockets of BCC structure being present for the higher damping simulation.

In Figure 7d, the higher damping simulation does not experience a grain growth similar to the benchmark sim-

ulation, with many fragmented grains and disordered atoms being present. By Figure 7e, the vast majority of the cell is in the disordered phase. There are only a few pockets of BCC atoms still present within the box. This corresponds to Figure 6f which showed that the percentage of atoms in the BCC phase at 4 strains was 2%. Between 4 strains (7e) and 7 strains (7f), there is a noticeable grain growth, which is even more noticeable at 10 strains (7g), corresponding to a larger number of atoms transitioning into the BCC phase as per Figure 6f.

Previous studies [70, 71] consider DRV to be the only dynamic recovery method in ferritic steels. However, the data presented in Figures 6 and 7 appears to show that DRX mechanisms are at play, which agrees with the observations made by Tsuji *et al.* [72], which confirmed the occurrence of DRX in BCC iron.

Comparing Figure 7e - 7g, the few remaining grains at 4 strains grow much larger and recrystallisation occurs. This process continues to make even larger grains at 10 strains. This coincides with an increase in the percentage of BCC phase, as shown in 6f. Interestingly, previous analysis of Figure 6c showed that the grain number plateaued at around 3 strains. As such, we further suggest that the process of DRX is present, as the grain number stays constant whilst the BCC structure continues to recover.

A larger damping parameter fundamentally means that the quenching rate is faster. This means that atoms lose their kinetic energy much more quickly, and get stuck in a disordered state. As shown in Figure 7c and 7d, the higher damping simulation experiences recrystallisation, similar to the benchmark simulation, but not to the same extent. It is not until a larger shear strain is applied that the atoms revert into a disordered state, as shown in Figure 7e. This is confirmed by looking at Figure 6f again, whereby there is an evident recovery of the BCC phase from the minimum at 0.27 strain, to 17% BCC at 0.44 strain. This is followed by a return to the disordered phase. It is not immediately evident why the atoms return to the disordered state post recrystallization. In the following section, we will attempt to outline a possible explanation for this.

As previously mentioned, the system is quenched at a higher rate for the higher damping simulation which causes many atoms to remain in the disordered phase. This essentially means after recrystallisation, the grain sizes are tiny and the grain boundary volume is large. As such, the dislocations formed as a result of shearing are heavily constrained within small grains [76] and more readily meet and annihilate at the grain boundaries. This is evident from Figure 6e which shows an increase in dislocation density up to $6.0 \times 10^{-4}/\text{\AA}^2$ post recrystallisation, followed by a quick drop in dislocation density, whereby the value is 0 at around 4 strains.

As dislocations are annihilated at grain boundaries and an increasing number of atoms enter a disordered state, the percentage of BCC structure decreases. The growth in grain size for the higher damped simulation provides

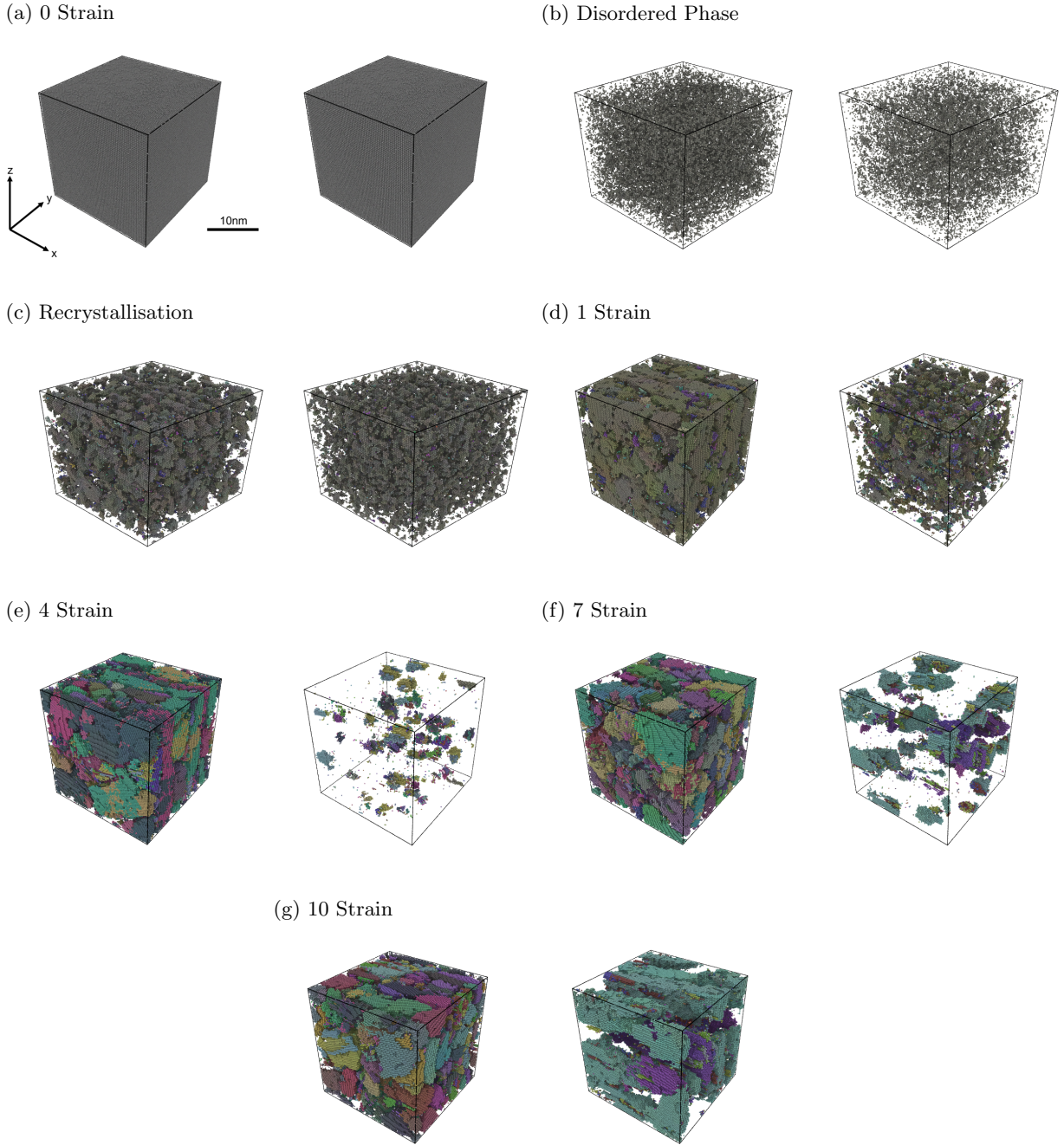


FIG. 7: Grain refinement process for different damping parameter simulations. Atoms are coloured according to atomic crystal orientations. Strain rate $d\varepsilon/dt = 1/33.5 \text{ ps}^{-1} \approx 2.985 \times 10^{10} \text{ s}^{-1}$. Left - Benchmark simulation with damping parameter $\gamma = 6.875 \text{ eV fs } \text{\AA}^2$; Right - Higher damping simulation with damping parameter $\gamma = 68.75 \text{ eV fs } \text{\AA}^2$.

the necessary grain volume for the propagation of dislocations, and an increase in dislocation density can be observed with the increase in BCC structure. It is also possible that, since there are many highly disordered atoms that manifest as grain boundaries, the free energy in the simulation is high, which drives the recrystallisation.

D. Strain Rate

The effect of strain rate was explored. We performed simulations at a shear strain rate which is 10 times slower than the benchmark simulation, whilst keeping other parameters unchanged. Figure 8 shows various properties

as a function of strain at normal and slow strain rates.

In Figure 8a and 8b, the initial kinetic energy spike is not as pronounced for the slower strain rate simulation. Whilst the benchmark simulation experiences an increase from 0.039 eV/atom to 0.072 eV/atom, the slower rate simulation only shows an increase from 0.039 eV/atom to 0.056 eV/atom. Furthermore, the spike for the benchmark simulation begins at 0.27 strain and peaks at 0.3 strain, whilst the slower rate simulation experiences a rise starting at 0.24 strain, and peaking at 0.25 strain. After the initial increase and subsequent decrease in kinetic energy, the slower rate simulation plateaus at a lower kinetic energy of around 0.039 eV/atom, compared with the benchmark simulation at 0.042 eV/atom.

The difference in the potential energy is shown in Figure 8c and 8d. Both simulations have identical trajectories in the initial stage. However, the slower rate simulation reaches the peak in potential energy at an earlier stage than the benchmark. The benchmark simulation peaks at -3.73 eV/atom at 0.27 strain, while the slower rate simulation peaks at -3.78 eV/atom at a strain of 0.24. This is followed by a rapid decrease for both simulations. The slower rate simulation decreases and plateaus at a lower potential energy, i.e. -3.95 eV/atom, than the benchmark, i.e. -3.89 eV/atom. The von Mises stress again correlates to the potential energy as shown in Figure 8f.

Though we can observe grain refinement in the benchmark simulation, this does not occur in the slower rate simulation, as shown in Figure 8e. The previously observed large spike in grains for the benchmark simulation does not occur in the slower rate simulation. Whilst there is a smaller initial peak of 80 grains at 0.27 strain for the slower rate simulation, this does not result in the formation of a largely polycrystalline structure, and after 0.38 strain, a single grain is present. This is contrary to the data obtained for the benchmark, and other previously discussed simulations that experienced the generation of many nanocrystalline grains.

This difference is also inferred by Figure 8i which compares the percentage of atoms in the BCC phase as a function of strain. A highly disordered state is observed for the benchmark simulation at 0.27 strain, where only 7% of the atoms are in the BCC phase, followed by a recovery where around 50% of the atoms remain in the BCC phase. The slower rate simulation also experiences this disordered state, but not to the same extent as the benchmark. At 0.24 strain, 37% of the atoms in the slower rate simulation are in the BCC phase, which is 30% more than the lowest benchmark value. Furthermore, the vast majority of the atoms regain their BCC phase, with the percentage of BCC atoms plateauing at around 93%. This is logical as the structure in the slower rate simulation is largely a single crystal, and there are no grain boundaries in the highly disordered state.

Various differences between the simulations are observed when analysing the dislocation densities in Figure 8g and 8h. After a shear strain of 0.27, the dislocation

density for the benchmark simulation gradually increases up to around $2.6 \times 10^{-3}/\text{\AA}^2$ at 0.82 strain, after which it decreases to $1.2 \times 10^{-3}/\text{\AA}^2$ at around 2 strains before plateauing at $1.6 \times 10^{-3}/\text{\AA}^2$. However, in the slower rate simulation, dislocation densities show a rapid increase to $3.6 \times 10^{-3}/\text{\AA}^2$ at 0.3 strain followed by a decrease to around $1.2 \times 10^{-3}/\text{\AA}^2$ at 1.6 strain. After this point, the dislocation densities for the simulations stay fairly similar, with the benchmark simulation having a slightly higher dislocation density with continued shearing.

A visual representation of dislocation density is shown in Figure 9 in pairs. The left-hand side is the normal rate, while the right-hand side shows the slower rate simulation. The dislocations are colour-coded in the same way as Figure 3. During recrystallisation, in Figure 9a, the benchmark simulation shows few dislocation lines, and they are sparse and disconnected. However, in the slower rate simulation, the dislocation density is much higher with a dislocation network being formed. This is in agreement with Figure 8h which depicts a large dislocation density at recrystallisation for the slower rate simulation compared with the benchmark.

At 1 strain (Figure 9b), a significant increase in dislocation density is observed within the benchmark cell. In contrast, the slower rate simulation cell displays a reduction in dislocation density, consistent with the findings in Figure 8h. From 1 strain (Figure 9b) to 10 strain (Figure 9e), the dislocation pattern in each simulation persists. The benchmark simulation shows small dislocation lines, with dislocation pile-ups attributed to grain boundary interactions. In contrast, the slower rate simulations display long dislocation lines, contributing to the formation of an extensive dislocation network. This behaviour persists due to the absence of grain boundaries constraining dislocation motion within the slower rate simulation cell.

The slower rate simulation does not experience the formation of polycrystals as with the benchmark simulation. During the initiation of plastic deformation, many dislocation loops are formed, which causes a large spike in dislocation density, as observed in Figure 9a. These loops do not form in the benchmark simulations as the presence of highly disordered atoms which manifests as grain boundaries. Polycrystalline grains limit the volume in which the dislocations can form, resulting in the observed short dislocation lines. With increased strain, the dislocations in the slower rate simulation are allowed to evolve and are not annihilated as there are no grain boundaries. Instead, as shown in Figure 9, they combine and form a large network of long dislocations. The presence of grain boundaries does not permit this phenomenon to occur in the benchmark simulation, so short dislocations are observed.

We may speculate the reason why the slower strain rate simulation does not experience the same polycrystal formation as the benchmark simulation. The kinetic energy does not increase to the same degree in the slower rate simulation, which could point to fewer atoms being able to accelerate within the lattice. As such, many atoms

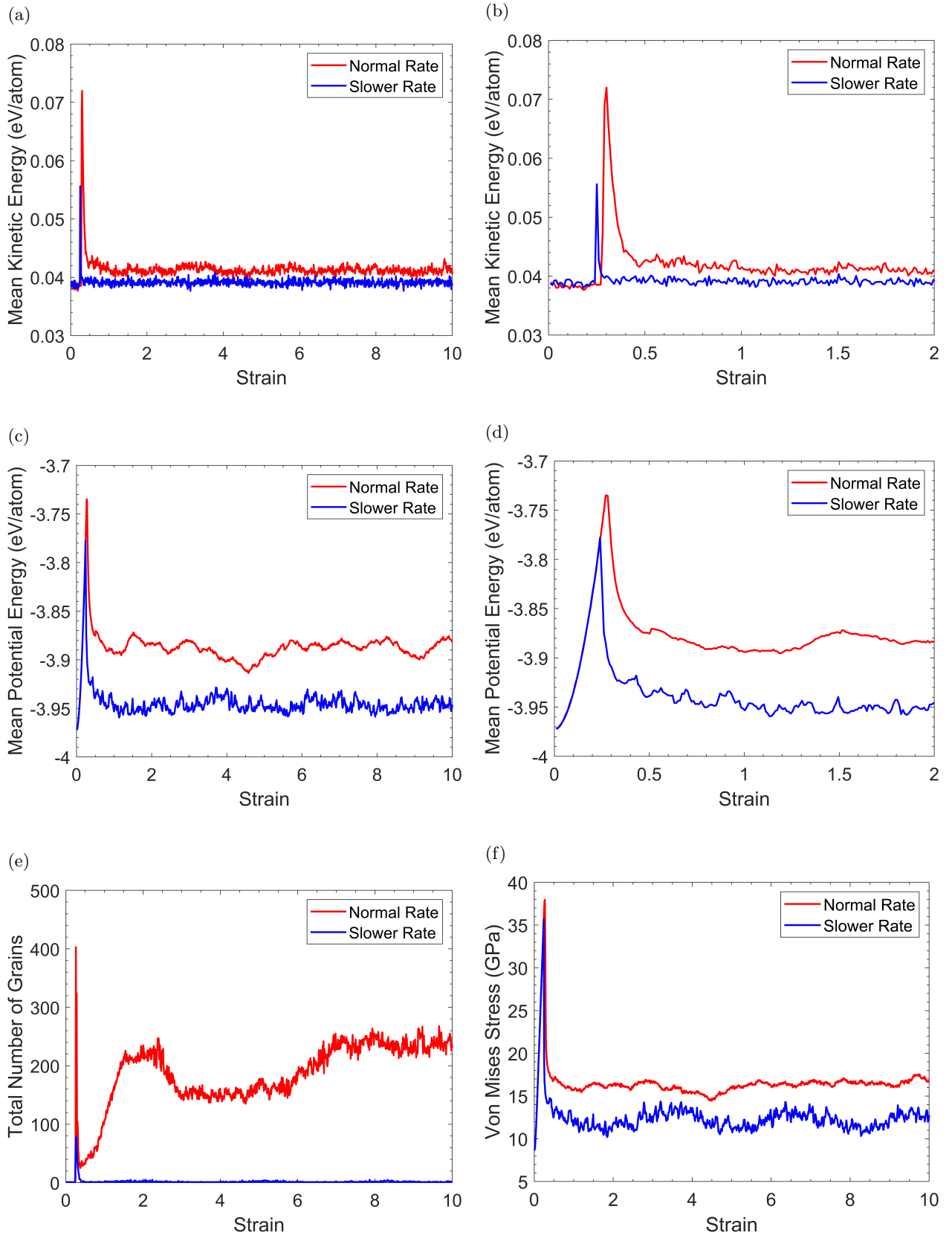


FIG. 8: Simulation data plotted as a function of strain using different strain rate. Damping parameter $\gamma = 6.875 \text{ eV fs } \text{\AA}^2$. Strain rate $d\varepsilon/dt = 1/33.5 \text{ ps}^{-1} \approx 2.985 \times 10^{10} \text{ s}^{-1}$ for Red line and strain rate $d\varepsilon/dt = 1/335 \text{ ps}^{-1} \approx 2.985 \times 10^9 \text{ s}^{-1}$ for Blue line. (a) Kinetic Energy (b) Kinetic Energy up to 2 strains (c) Potential Energy (d) Potential Energy up to 2 strains (e) Number of Grains (f) Von Mises Stress (g) Dislocation Density (h) Dislocation Density up to 2 strains (i) percentage of BCC structure.

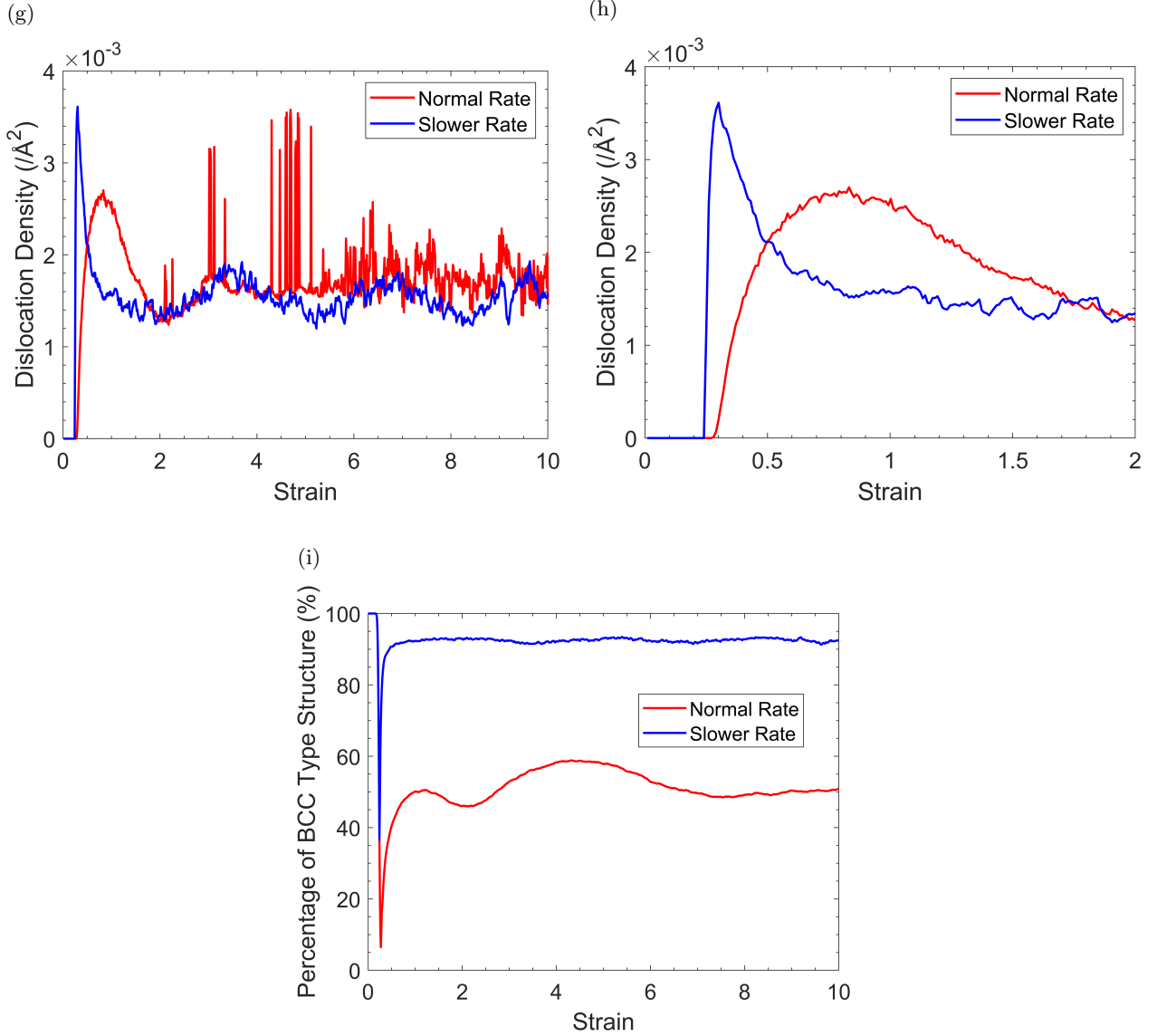


FIG. 8: Simulation data plotted as a function of strain using different strain rate. Damping parameter $\gamma = 6.875$ eV fs \AA^2 . Strain rate $d\varepsilon/dt = 1/33.5$ ps $^{-1} \approx 2.985 \times 10^{10}$ s $^{-1}$ for Red line and strain rate $d\varepsilon/dt = 1/335$ ps $^{-1} \approx 2.985 \times 10^9$ s $^{-1}$ for Blue line. (a) Kinetic Energy (b) Kinetic Energy up to 2 strains (c) Potential Energy (d) Potential Energy up to 2 strains (e) Number of Grains (f) Von Mises Stress (g) Dislocation Density (h) Dislocation Density up to 2 strains (i) percentage of BCC structure.

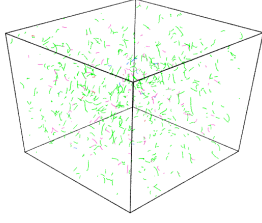
will retain their original structure and this is confirmed in Figure 8i. This increase in kinetic energy comes at a lower strain for the slower rate simulation which results in a smaller increase in potential energy. Ultimately, this means that fewer atoms are in the disordered state for the slower rate simulation, and it appears that, with increased strain, it is more energetically favourable for the atoms to recrystallise back into a single crystal structure rather than a polycrystalline one.

DRV mechanisms appear to be present within the slower rate simulation, and the longer time scale gives dislocations more time to recover [77]. This means that

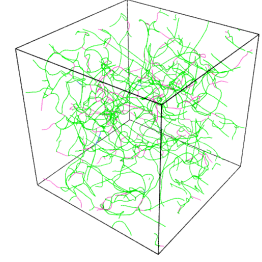
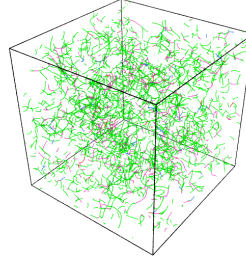
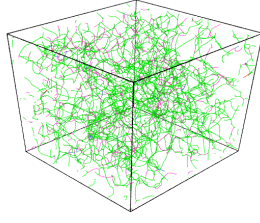
the dislocations are less susceptible to pile up, and are unable to begin the process of forming grain boundaries, again limiting the grain refinement. It may also be possible that the dislocations are simply unable to pile up, because the large dislocation network, on different slip planes, impedes each other. When in close contact, the strain field surrounding a dislocation repels other dislocations, which in turn interferes with their movement [78]. As their motion becomes more restrained, they are less able to come together and form LAGBs, blocking the process of grain refinement.

Experimental works suggest that a lower strain rate

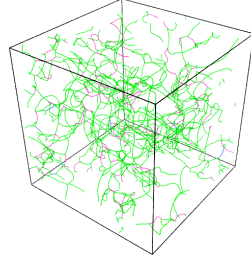
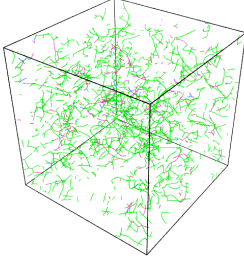
(a) Recrystallisation



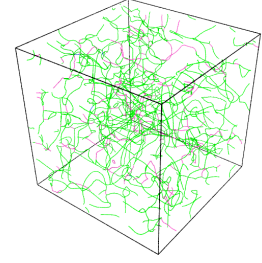
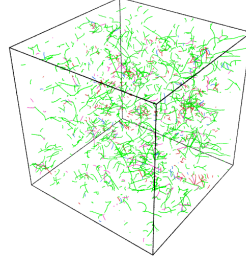
(b) 1 Strain



(c) 4 Strains



(d) 7 Strains



(e) 10 Strains

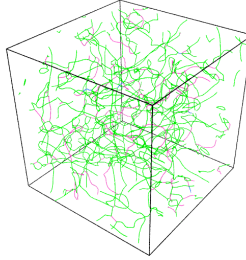
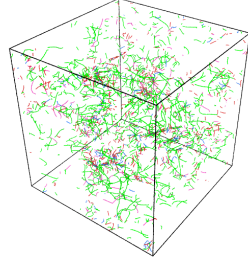


FIG. 9: Dislocation network comparison for different strain rate simulations. Damping parameter $\gamma = 6.875 \text{ eV fs } \text{\AA}^2$. Green dislocation lines $\mathbf{b} = \frac{1}{2}\langle 111 \rangle$ and pink dislocation lines $\mathbf{b} = \langle 100 \rangle$. Left - Benchmark simulation with strain rate $d\varepsilon/dt = 1/33.5$; Right - Slower rate simulation with strain rate $d\varepsilon/dt = 1/335$.

correlates to a larger mean grain size [64, 66] and it is possible that the simulation cell size is the limiting factor. In the future, it may be beneficial to carry out such shearing simulations with a much larger number of atoms to ascertain whether the cell size is a limiting factor.

E. Carbon Impurities

At which point, may one consider the carbon impurity content to be negligible? Some sources point to a maximum carbon content of 0.006% [79] whilst others argue that a carbon content as low as 0.001% can already immensely affect the properties of iron [80]. Ferritic/martensitic steels that have been selected for fusion applications typically contain less than 0.15% carbon [81]. The atomic size of carbon is small enough that

the atom can enter the iron lattice as an interstitial solute atom [82]. Experiments showed that carbon can greatly influence the microstructural behaviour of iron. For example, Stein [83] showed that the dislocation velocity exponent increases in iron with an increase in carbon content when held at room temperature. This alters the yield point and rate of crack propagation within the material. Molecular dynamics simulations have also been carried out which show the effect of carbon interstitials. Carbon atoms can block dislocation motion in an iron simulation cell [84].

In the current work, we inserted 102 carbon atoms into the simulation cell, that is 100 appm or 0.01 atomic %. We attempt to understand the effect of carbon interstitial atoms on the formation of nanograins under shear strain in iron.

Figure 10 shows various simulation properties with and

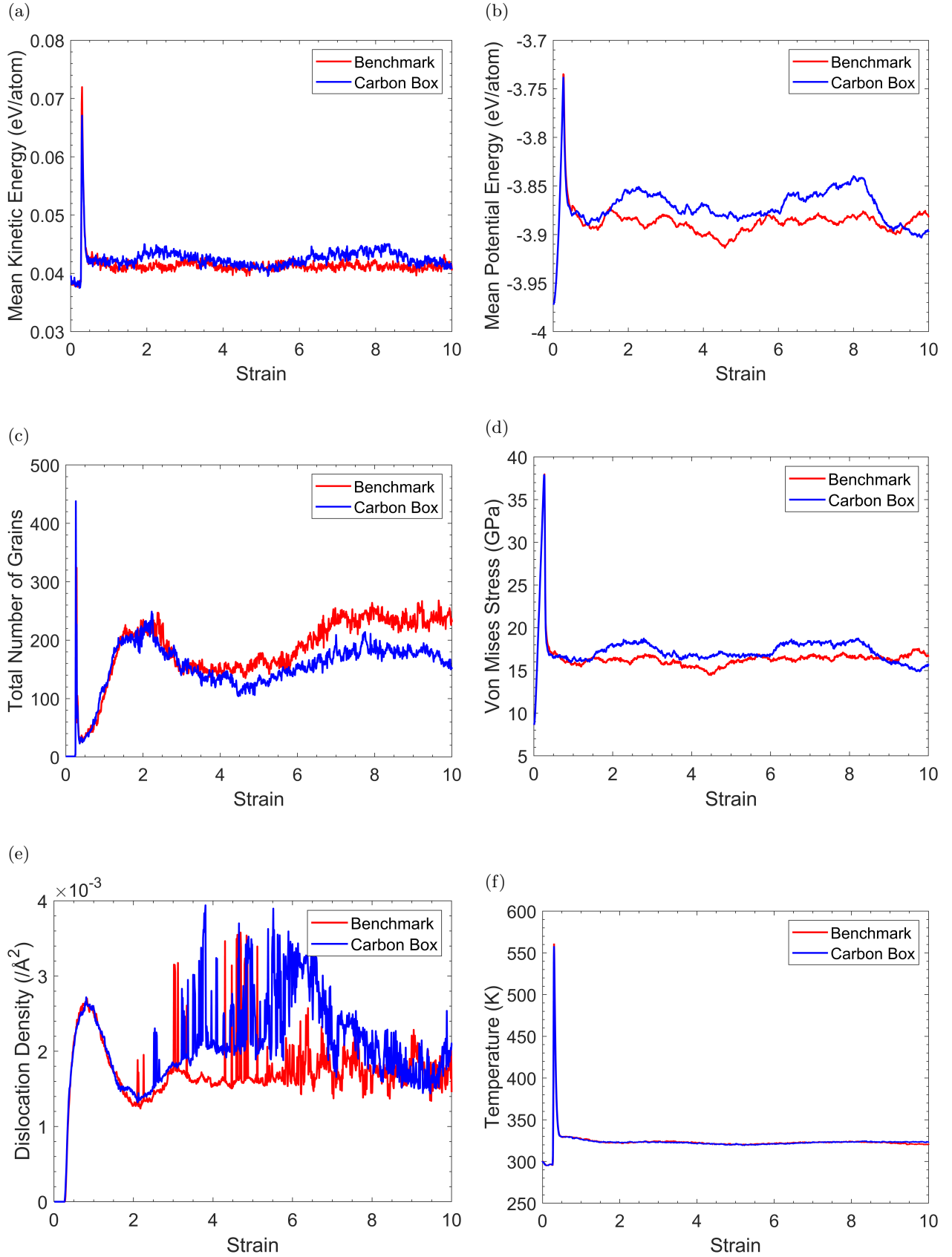


FIG. 10: Simulation data plotted as a function of strain for benchmark and carbon-containing simulations. Strain rate $d\varepsilon/dt = 1/33.5 \text{ ps}^{-1} \approx 2.985 \times 10^{10} \text{ s}^{-1}$ and damping parameter $\gamma = 6.875 \text{ eV fs } \text{\AA}^2$. The red line is for the benchmark and the blue line is for 100 appm carbon in iron simulation. (a) Kinetic Energy (b) Potential Energy (c) Number of Grains (d) Von Mises Stress (e) Dislocation Density (f) Temperature.

without carbon impurities. Figure 10a shows the differences in kinetic energy between the simulations. The benchmark simulation experiences a rapid increase in kinetic energy, from 0.039 eV/atom at 0.27 strain, to 0.072 eV/atom at 0.3 strain, before rapidly decreasing and plateauing at 0.042 eV/atom. Similarly, the kinetic energy for the carbon-containing simulation increases from 0.039 eV/atom at 0.27 strain, to 0.067 eV/atom at 0.3 strain, before rapidly decreasing. Hence, the difference in maximum kinetic energy between the simulations is around 0.005 eV/atom. Furthermore, both simulations experience kinetic energy reductions to 0.042 eV/atom at 0.32 strain. Whilst the benchmark simulation plateaus at this point, the kinetic energy for the carbon-containing cell becomes sinusoidal with continued strain. We observe two local maxima of 0.045 eV/atom at around 2 and 8 strains.

In Figure 10b, the behaviour of the potential energy is nearly identical for both simulations up to 1 strain. Both cells experience a rapid increase from 0 strain, followed by a rapid decrease at 0.27 strain, to a value of around -3.89 eV/atom at around 0.82 strain. However, the potential energy of the carbon-containing simulation increases again from this point, reaching -3.85 eV/atom at 2 strains, before decreasing slightly, and once again increasing to -3.84 eV/atom at 8 strains. Note that these increases in potential energy also correspond to local maxima in kinetic energy. This trend is also shown in Figure 10d, which shows the von Mises stress for both cells.

Figure 10c shows the number of grains found in each simulation cell. There are some minor differences between the two simulations. The initial grain number increases up to around 400 for the benchmark simulation, whilst the maximum number of grains found in the cell with carbon atoms is 440, a difference of 40 grains. Nevertheless, both simulations experience a nearly identical trajectory from 0.27 strain to 3 strains. After this point, the number of grains present in the benchmark simulation is noticeably larger than the carbon-containing cell. For example, at 8 strains, the number of grains found in the benchmark simulation is around 260, whilst the carbon-containing cell only has around 210.

A similar trend is observed when considering the dislocation densities of the simulations in Figure 10e. Again, the trajectories of the simulations are nearly identical up to 3 strains. With continued shearing, the dislocation density of the carbon-containing cell is noticeably larger, until the values become similar for both simulations at around 8.5 strains.

In Figure 10f, it is interesting to observe identical simulation temperatures for the benchmark simulation and carbon-containing simulation, whilst the kinetic energy between them is not identical. It is not immediately apparent what could cause this rise in kinetic energy, as there is no simultaneous rise in temperature.

Figure 11 shows the mean kinetic energy broken down by atom type for the carbon-containing simulation. Evi-

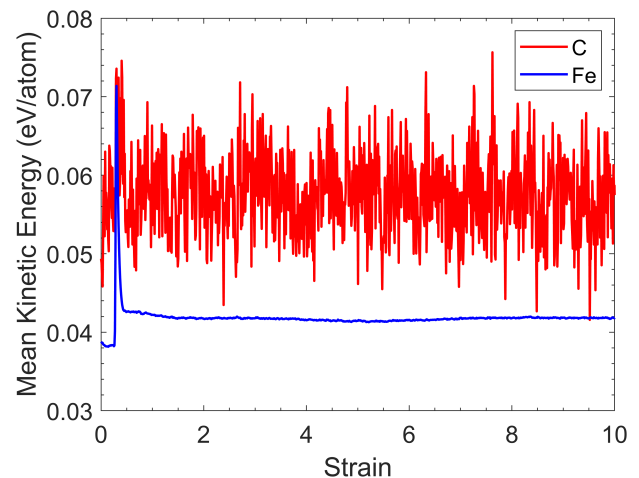


FIG. 11: Kinetic energy based on atom type for carbon-containing simulation. Strain rate $d\varepsilon/dt = 1/33.5 \text{ ps}^{-1} \approx 2.985 \times 10^{10} \text{ s}^{-1}$ and damping parameter $\gamma = 6.875 \text{ eV fs } \text{\AA}^2$.

dently, the carbon atoms have higher kinetic energy and the energy fluctuation is large. This suggests a great deal of carbon atoms experience rapid acceleration and deceleration with shear, implying their movements throughout the box.

Carbon atoms can move within the material by jumping between interstitial sites through diffusion [85]. Figure 11 suggests that these carbon atoms may overcome the diffusion energy barrier continuously causing them to rapidly move to other interstitial sites, which is realized as a larger spread of kinetic energy.

The work done by Wert [86] managed to characterise the diffusion coefficient of carbon in iron as a function of the temperature, and subsequent work has pointed to a diffusion barrier of around 0.87 eV for carbon in iron at room temperature [87]. This is further reinforced by the work of Tapasa *et al.* [88], which also found that the activation energy of C migration in Fe to be 0.82 - 0.86 eV, which is much larger than the kinetic energy spikes in Figure 11. Fu *et al.* [89] performed density functional theory (DFT) calculations to explore the migration energy of C atoms in Fe. They found that C atoms will migrate from neighbouring octahedral sites through a tetrahedral site, with an energy barrier of 0.87 eV. This value agrees with the work of Wert [86] and Tapasa [88]. Other DFT calculations have also obtained similar values [90, 91].

Analyzing Figure 10b, we observe higher overall potential energy in the carbon-containing cell due to the presence of carbon as an interstitial solute in the lattice. This inclusion distorts the iron lattice, leading to higher potential energy and von Mises stress (Figure 10d). Two local energy spikes appear at 2 and 8 strain, coinciding with kinetic energy peaks (Figure 10a). These conditions resemble the Snoek effect [92], where under stress, carbon atoms migrate along the stress axis, reducing lattice strain energy [93]. This movement boosts their kinetic

energy and the system’s kinetic energy. This aligns with Snoek relaxation for Fe-C, occurring at low temperatures, as shown in Figure 10f. Hence, the potential energy reduction mechanism in the carbon-containing cell is similar to Snoek relaxation.

In Figure 10e, the carbon-containing cell initially shows a higher dislocation density compared to the benchmark simulation up to around 8.5 strains, after which they become similar. Carbon, behaving as a solute interstitial in the lattice, impedes dislocation motion [94]. This prohibits dislocations from gliding effectively within the lattice, hampering their movement toward grain boundaries and limiting the formation of new LAGBs. This restraint likely contributes to the lower overall grain count in the carbon-containing cell, as shown in Figure 10c. Essentially, hindered dislocation glide and limited LAGB formation slow grain refinement, yielding higher dislocation density. Moreover, dislocations carry excess free energy [60], likely contributing to the higher overall potential energy in the carbon-containing cell (Figure 10b). Interestingly, the potential energy notably decreases beyond 8 strain, even surpassing the benchmark simulation, aligning with the reduction in dislocation density in the carbon-containing box.

IV. CONCLUSION

Nanocrystalline formation in iron under high shear strain has been observed through molecular dynamic simulations. The process of nucleation and growth of nanograins during the shearing involves a disordered state, recrystallization, and grain coarsening. The disordered state is caused by a sudden surge in kinetic energy gained from the drop in potential energy, which was high and unstable due to shearing. Following this, energy is dissipated into the environment, mimicked by the thermostat. Atoms rearrange locally to achieve energetically favourable configurations that lead to recrystallization and grain coarsening.

We also examined the influence of various factors, such as thermostat temperature, heat dissipation rate, shear strain rate, and carbon content. Simulations at higher temperatures still experience nanocrystalline formation, but with larger and longer grains forming. A faster rate of heat dissipation altered the grain refinement process. This also involved a disordered state, followed by recrystallization. However, dynamic restoration mechanisms were observed to play a major role in nanocrystalline formation. Simulations with a slower strain rate did not produce nanocrystalline material, with only a single crystal structure being observed. The inclusion of carbon interstitial atoms had a minor effect on nanocrystalline formation, with the process of grain refinement being identical to that of the pristine material. Nonetheless, a smaller number of grains were generally observed for the carbon-containing simulations.

The current simulations demonstrate a possible mech-

anism of nanograin formation using high-shear methods, which we have not found reported in the literature.

V. DATA AVAILABILITY

All input scripts and simulation data presented in the current work are available at *A link will be provided after the review process and before publication.*

ACKNOWLEDGMENTS

The authors gratefully acknowledge the Department of Engineering Science at the University of Oxford for their contribution to the funding of the project. This work has been carried out within the framework of the EUROfusion Consortium, funded by the European Union via the Euratom Research and Training Programme (Grant Agreement No 101052200 — EUROfusion) and from the EPSRC [grant number EP/W006839/1]. To obtain further information on the data and models underlying this paper please contact PublicationsManager@ukaea.uk. Views and opinions expressed are however those of the author(s) only and do not necessarily reflect those of the European Union or the European Commission. Neither the European Union nor the European Commission can be held responsible for them. The authors acknowledge the use of the Cambridge Service for Data Driven Discovery (CSD3) and associated support services provided by the University of Cambridge Research Computing Services (www.csd3.cam.ac.uk) in the completion of this work. This work used the ARCHER2 UK National Supercomputing Service (<https://www.archer2.ac.uk>).

Appendix A: Further analysis

1. Slip Systems

To analyze the slip systems within the current orientation, we calculated the Schmid factor [95]. We apply a constant shear strain in the xy direction, resolving to principal strains at 45° . Although the stress magnitude changes as the simulation progresses, normalizing the applied stress direction to $\sigma = [1\bar{1}0]$ is feasible. With shear strain confined to the xy direction and periodic boundary conditions in place, a plane stress is assumed. In BCC structures like α -iron, slip direction predominantly aligns with the $\langle 111 \rangle$ family, while slip planes encompass the $\{110\}$, $\{112\}$, and $\{123\}$ families for Fe [96, 97]. Using these stress values alongside slip planes and directions, we calculated the Schmid factor using:

$$m = \cos(\phi)\cos(\lambda), \quad (\text{A1})$$

where m is the Schmid factor, ϕ is the angle between the normal of the slip plane and the direction of applied

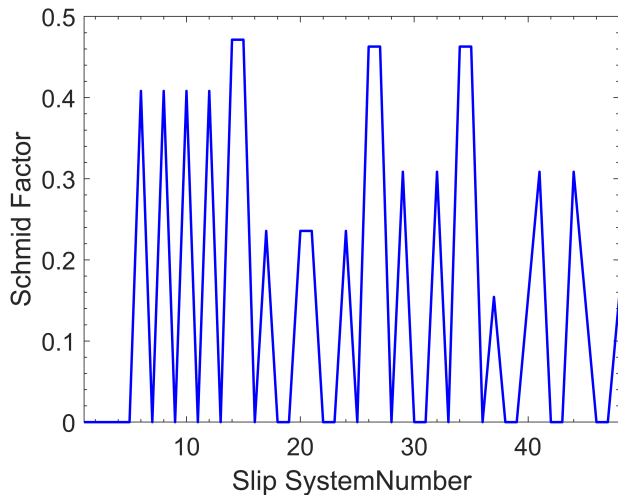


FIG. 12: Schmid Factor for all slip systems in BCC system under shear strain.

stress, and λ is the angle between the direction of applied stress and the slip direction.

The Schmid factor can be calculated using:

$$\cos(\phi) = \frac{\vec{\sigma} \cdot \vec{n}}{|\vec{\sigma}| |\vec{n}|}, \quad (\text{A2})$$

$$\cos(\lambda) = \frac{\vec{\sigma} \cdot \vec{d}}{|\vec{\sigma}| |\vec{d}|}, \quad (\text{A3})$$

where \vec{n} is the vector normal to the slip plane, and \vec{d} is the vector in the direction of the slip.

There is a total of 48 slip systems in BCC metal. A full list of these can be found in [98]. The Schmid factor was calculated for each system and this is shown in Figure 12.

Analyzing Figure 12, we discover a multitude of potential slip systems that can activate within the system when the crystal is oriented along $x = [100]$. This observation may shed light on why the grain refinement process initiates with numerous atoms entering a highly disordered state. During the shearing of the cell, a diverse set of slip systems is simultaneously engaged. Upon reaching the critical stress point, this leads to a mixing of atoms, inducing high disorientation due to the involvement of multiple slip directions. Subsequent quenching then triggers recrystallization.

2. Further Dislocation Analysis

We performed additional DXA calculations after eliminating grain boundaries. This is done by removing atoms that are sitting close to grain boundaries. We adopt the code developed by Mason [62, 99]. It provides the distance d of each atom to the nearest grain boundary. Atoms with $d < 1$ Å were excluded, followed by a subsequent DXA calculation. Figure 13 displays the analysis

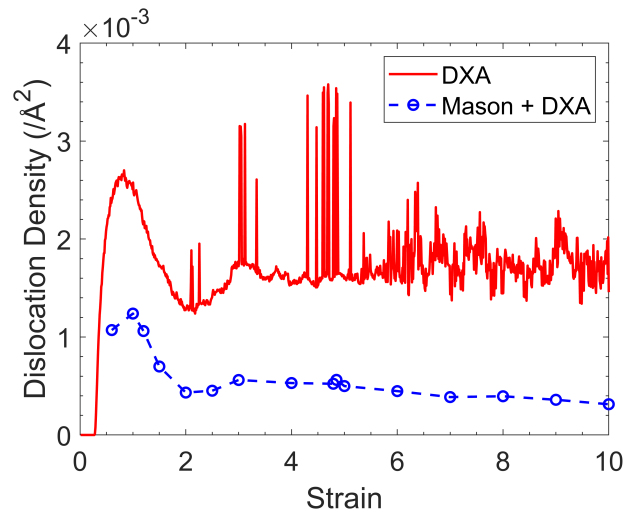


FIG. 13: Dislocation density comparison between standard DXA and DXA carried out when $d < 1$ atoms removed.

outcomes.

Figure 13 demonstrates that the standard DXA tends to overestimate dislocation density, possibly due to grain boundaries. Dislocations can glide and accumulate at grain boundaries, with some leading to the formation of LAGBs [4, 8–10]. It's likely that DXA interprets certain LAGBs as dislocation lines, accounting for the discrepancy in dislocation count. Specifically, conspicuous spikes in dislocation density around 4.8 strain are observed, absent when $d < 1$ atoms are excluded. Thus, we conclude that the standard DXA encompasses dislocation pile-ups and LAGBs in its dislocation density computation. Nevertheless, the current analysis remains a robust foundation for comparing various simulations.

3. What Constitutes a Grain?

In this work, we considered a minimum grain size of 50 atoms when determining the number of grains present within the system. This number was selected as it allowed us to observe the transition to the disordered state and the subsequent recrystallisation clearly. Nevertheless, Figure 14 shows the comparison of grain numbers for the benchmark simulation with different numbers of atoms selected to form the minimum grain size. The Ovito default of 100 atoms was selected for comparison, as was 5,558 atoms, which corresponds to a 5nm diameter spherical grain. A 5nm grain corresponds to a minimum grain size which can accurately be resolved using transmission Kikuchi diffraction (TKD, or t-EBSD) [100], allowing comparisons with future experimental HPT data.

Figure 14 shows that the number of grains between the 50-atom and 100-atom analyses largely follow the same trajectory. At 0.27 strain, our-50 atom analysis showed 400 grains whilst the 100-atom analysis showed 215. This

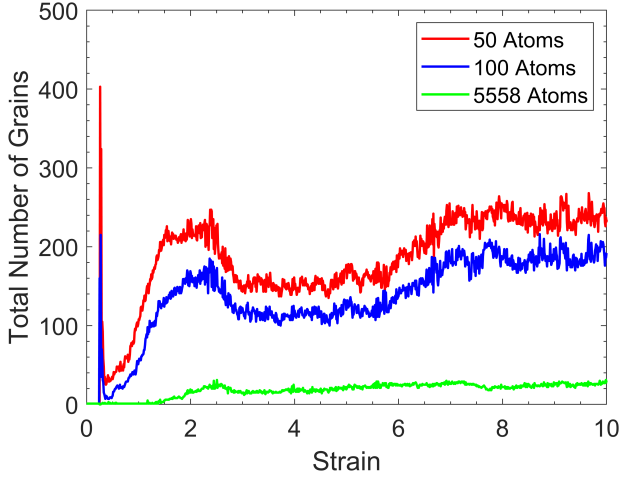


FIG. 14: Total number of grains based on minimum number of atoms per grain.

means that 185 grains were found to have less than 100 but more than 50 atoms at this point. This further suggests that the spike is caused by a highly disordered state of the atoms whereby only small pockets of BCC phase atoms remain, which is flagged as a grain. At this strain value, the 5nm grain analysis cannot pick up any grains due to the highly disordered state, and the grain number is shown as 0. After 2 strains, the 50- and 100-atom trajectories follow the same trajectory, however, there is always a difference of around 40 grains between the analyses. Therefore, we conclude that there are always around 40 grains in the simulation cell which have less than 100 atoms but more than 50. Interestingly, the 5nm grain analysis does not follow the same trajectory, and instead hovers around 1 grain up to around 1.37 strain. After this point, the grain number increases for the 5nm analysis, as shown in Figure 14. A local maximum of grain number is reached at around 2.5 strain, with 30 grains being present. This is followed by a minor decrease, after which the grain number sits steadily at around 25 after 4 strains. As such, we observe that the process of grain refinement still occurs if we define a grain with a minimum of 5,558 atoms.

It further supports our hypothesis that the transition of atoms into the disordered state, followed by a recrystallisation and grain growth, is a major mechanism of grain refinement. It is clear that up to 1.37 strains, all of the grains are small, with many containing less than 100 atoms. Through the processes of grain growth described above, the grains expand, causing the 5nm analysis value to increase. This analysis saturates at around 25-30 grains and any subsequent changes in the simulation cell with shear occur through small grain processing.

By increasing the minimum number of atoms that constitute a grain, we can compare the effects of temperature and carbon on the formation of experimentally observable grains. Figure 15 shows the number of 5nm spherical grains found in different temperature simulations and

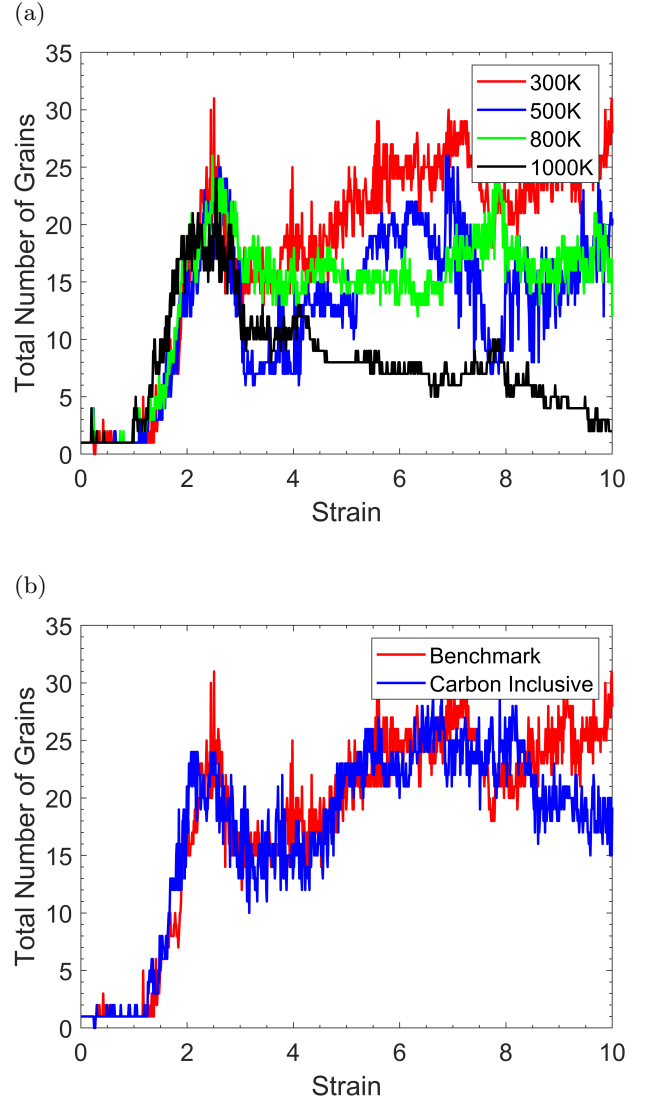


FIG. 15: Number of 5nm spherical grains found in the simulations; (a) Dependence of temperature on 5nm grains, and (b) Dependence of carbon inclusion on 5nm grains.

carbon-containing simulations.

In Figure 15a, there is no initial spike in 5nm grains for any simulation, and the trajectories of the different simulations are largely similar until around 2.5 strain. This is contrary to the data shown in Figure 4f which shows that the 300 K simulation has the most grains at this point, suggesting that at 300 K, the grain numbers are increased due to the presence of many small grains. We also notice that the 1000 K simulation has around 2 grains larger than 5nm at 10 strain, which is visible by considering Figure 5g. Ultimately, the 300 K simulation still shows the largest number of grains overall. However, this is not to the same extent as in Figure 4f, again suggesting that the shearing process stimulates the pro-

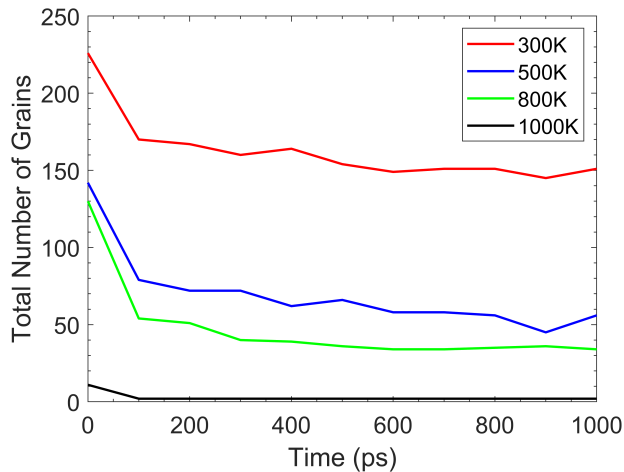


FIG. 16: Number of grains present in different temperature simulations after thermalising.

duction of many small grains in the 300 K simulation. Nevertheless, the 500 K and 800 K simulations also have many small grains, and this is visible by comparing the data in Figure 15a to Figure 4f. For example, at 6 strain, the total number of grains present for the 500 K simulation is 120 and that number drops to 20 when considering only 5nm grains.

Figure 15b also shows the comparison of 5nm grains between the benchmark and carbon-containing simulation. We show here that the deviation in grain number observed in Figure 10c does not occur when consider-

ing 5nm grain, up to 8.5 strain. This suggests that the benchmark simulation has many smaller grains than the carbon-containing simulation. After 8.5 strain, we notice that the carbon-containing simulation begins to dip in grain number whilst the benchmark simulation cell rises.

4. Thermal Stability of Grains

It was important to assess the stability of the newly formed grains to assess their usefulness for future simulations. The benchmark simulation and the variable temperature simulations from Section 3 were chosen for assessment. These cells were thermalised for 1ns using the NPH ensemble, with the Langevin thermostat keeping the temperature at 300 K, 500 K, 800 K, and 1000 K. Figure 16 shows the total number of grains present after the 1ns run time for each simulation cell. For the purposes of this comparison, the minimum grain size was taken as 50 atoms.

Inspection of Figure 16 shows that all cells follow similar trends. There is first a reduction in the number of grains found in the cell, after which the number of grains stabilises after around 700 ps of thermalisation. The 300 K, 500 K, and 800 K simulations all stabilise at around 150, 56, and 35 grains, respectively. It is shown that the 1000 K simulation stabilises much earlier, at a value of 2 grains. As such, it is inferred that the nanocrystalline structure will remain stable at finite temperatures.

-
- [1] G. Govender, H. Möller, and O. Damm, 5.06 - semisolid processes, in *Comprehensive Materials Processing*, edited by S. Hashmi, G. F. Batalha, C. J. Van Tyne, and B. Yilbas (Elsevier, Oxford, 2014) pp. 109–134.
 - [2] K. M. Agarwal, R. K. Tyagi, V. K. Chaubey, and A. Dixit, Comparison of different methods of severe plastic deformation for grain refinement, *IOP Conference Series: Materials Science and Engineering* **691**, 012074 (2019).
 - [3] A. Zhilyaev, K. Oh-ishi, T. Langdon, and T. McNelly, Microstructural evolution in commercial purity aluminum during high-pressure torsion, *Materials Science and Engineering: A* **410-411**, 277 (2005), the Langdon Symposium: Flow and forming of Crystalline Materials.
 - [4] Y. Ito and Z. Horita, Microstructural evolution in pure aluminum processed by high-pressure torsion, *Materials Science and Engineering: A* **503**, 32 (2009), international Symposium on Bulk Nanostructured Materials: from Fundamentals to Innovation, BNM 2007.
 - [5] M. Jamalain, M. Hamid, N. De Vincentis, Q. Buck, D. P. Field, and H. M. Zbib, Creation of heterogeneous microstructures in copper using high-pressure torsion to enhance mechanical properties, *Materials Science and Engineering: A* **756**, 142 (2019).
 - [6] K. Bryła, J. Morgiel, M. Faryna, K. Edalati, and Z. Horita, Effect of high-pressure torsion on grain refinement, strength enhancement and uniform ductility of ez magnesium alloy, *Materials Letters* **212**, 323 (2018).
 - [7] S. M. Mohd Yusuf, Y. Chen, and N. Gao, Influence of high-pressure torsion on the microstructure and microhardness of additively manufactured 316l stainless steel, *Metals* **11**, 1553 (2021).
 - [8] M. Borodachenkova, W. Wen, and A. M. de Bastos Pereira, High-pressure torsion: Experiments and modeling, in *Severe Plastic Deformation Techniques*, edited by M. Cabibbo (IntechOpen, Rijeka, 2017) Chap. 4.
 - [9] W. Xu, J. Yu, L. Jia, C. Gao, Z. Miao, G. Wu, G. Li, and Z. Zhang, Grain refinement impact on the mechanical properties and wear behavior of Mg-9Gd-3Y-2Zn-0.5Zr alloy after decreasing temperature reciprocating upsetting-extrusion, *Journal of Magnesium and Alloys* **10**, 3506 (2022).
 - [10] X. Li and K. Lu, Refining grains of metals through plastic deformation: Toward grain size limits, *Accounts of Materials Research* **2**, 108 (2021), <https://doi.org/10.1021/accountsmr.0c00075>.
 - [11] M. J. Starink, X. G. Qiao, J. Zhang, and N. Gao, Predicting grain refinement by cold severe plastic deformation in alloys using volume averaged dislocation generation, *Acta Materialia* **57**, 5796 (2009).

- [12] M. Liu, H. Roven, X. Liu, M. Murashkin, R. Valiev, T. Ungár, and L. Balogh, Grain refinement in nanostructured al–mg alloys subjected to high pressure torsion, *Journal of Materials Science* **45**, 4659 (2010).
- [13] M. Borodachenkova, F. Barlat, W. Wen, A. Bastos, and J. Grácio, A microstructure-based model for describing the material properties of al–zn alloys during high pressure torsion, *International Journal of Plasticity* **68**, 150 (2015).
- [14] J. Luo, W. Yu, C. Xi, C. Zhang, and C. Ma, Preparation of ultrafine-grained gh4169 superalloy by high-pressure torsion and analysis of grain refinement mechanism, *Journal of Alloys and Compounds* **777**, 157 (2019).
- [15] W. Wu, M. Song, S. Ni, J. Wang, Y. Liu, B. Liu, and X. Liao, Dual mechanisms of grain refinement in a fecorni high-entropy alloy processed by high-pressure torsion, *Scientific Reports* **7**, 46720 (2017).
- [16] M. Isik, M. Niinomi, H. Liu, K. Cho, M. Nakai, Z. Horita, S. Sato, T. Narushima, H. Yilmazer, and M. Nagasako, Grain refinement mechanism and evolution of dislocation structure of co–cr–mo alloy subjected to high-pressure torsion, *MATERIALS TRANSACTIONS* **57**, 1109 (2016).
- [17] P. Verleysen, F. Van den Abeele, and J. Degriek, Numerical simulation of severe plastic deformation during high pressure torsion processing, in *SIMULIA, Proceedings* (2013) p. 9.
- [18] P. H. R. Pereira and R. B. Figueiredo, Finite element modelling of high-pressure torsion: An overview, *MATERIALS TRANSACTIONS* **60**, 1139 (2019).
- [19] H. S. Kim, Finite element analysis of high pressure torsion processing, *Journal of Materials Processing Technology* **113**, 617 (2001), 5th Asia Pacific conference on Materials processing.
- [20] S. C. Yoon, Z. Horita, and H. S. Kim, Finite element analysis of plastic deformation behavior during high pressure torsion processing, *Journal of Materials Processing Technology* **201**, 32 (2008), 10th International Conference on Advances in Materials and Processing Technologies.
- [21] X. Zhang, Z. Chen, and Y. Liu, Chapter 6 - constitutive models, in *The Material Point Method*, edited by X. Zhang, Z. Chen, and Y. Liu (Academic Press, Oxford, 2017) pp. 175–219.
- [22] P. Wei, H. Zhou, H. Liu, C. Zhu, W. Wang, and G. Deng, Investigation of grain refinement mechanism of nickel single crystal during high pressure torsion by crystal plasticity modeling, *Materials* **12**, 10.3390/ma12030351 (2019).
- [23] K. Frydrych and K. Kowalczyk-Gajewska, Grain refinement in the equal channel angular pressing process: simulations using the crystal plasticity finite element method, *Modelling and Simulation in Materials Science and Engineering* **26**, 065015 (2018).
- [24] H. Mecking, U. Kocks, and C. Hartig, Taylor factors in materials with many deformation modes, *Scripta Materialia* **35**, 465 (1996).
- [25] J. Schiøtz and K. W. Jacobsen, A maximum in the strength of nanocrystalline copper, *Science* **301**, 1357 (2003), <https://www.science.org/doi/pdf/10.1126/science.1086636>.
- [26] L. A. Merzhievsky, I. F. Golovnev, and E. I. Golovneva, Molecular-dynamic simulation of nanocrystal structure evolution under dynamic loading, AIP Conference Proceedings **1785**, 10.1063/1.4967018 (2016), 020002, https://pubs.aip.org/aip/acp/article-pdf/doi/10.1063/1.4967018/7485459/020002_1_online.pdf.
- [27] S. Kotrechko, A. Filatov, and A. Ovsjannikov, Molecular dynamics simulation of deformation and failure of nanocrystals of bcc metals, *Theoretical and Applied Fracture Mechanics* **45**, 92 (2006).
- [28] P. Wang, X. Yang, and D. Peng, Molecular dynamics investigation of the grain boundary migration hysteresis of nanocrystalline ni under cyclic shear loading, *Modelling and Simulation in Materials Science and Engineering* **25**, 025006 (2016).
- [29] G. Agarwal, G. Paun, R. R. Valisetty, R. Namburu, A. M. Rajendran, and A. M. Dongare, Atomistic study of deformation and failure behavior in nanocrystalline mg, *MRS Advances* **1**, 3859–3864 (2016).
- [30] A. Husain, P. La, Y. Hongzheng, and S. Jie, Molecular dynamics as a means to investigate grain size and strain rate effect on plastic deformation of 316 l nanocrystalline stainless-steel, *Materials* **13**, 10.3390/ma13143223 (2020).
- [31] A. Y. Nikonov, Molecular dynamics study of the behavior of single- and polycrystals of BCC Fe under shear loading conditions, AIP Conference Proceedings **2051**, 10.1063/1.5083456 (2018), 020213, https://pubs.aip.org/aip/acp/article-pdf/doi/10.1063/1.5083456/13354336/020213_1_online.pdf.
- [32] X. Guan, A. Liang, and P. Branicio, High pressure shear induced microstructural evolution in nanocrystalline aluminum, *Computational Materials Science* **203**, 111105 (2022).
- [33] N. Baluc, R. Schäublin, P. Spätig, and M. Victoria, On the potentiality of using ferritic/martensitic steels as structural materials for fusion reactors, *Nuclear Fusion* **44**, 56 (2003).
- [34] S. Zinkle and G. Was, Materials challenges in nuclear energy, *Acta Materialia* **61**, 735 (2013), the Diamond Jubilee Issue.
- [35] S. J. Zinkle and J. T. Busby, Structural materials for fission & fusion energy, *Materials Today* **12**, 12 (2009).
- [36] F. A. Garner, M. B. Toloczko, and B. H. Sencer, Comparison of swelling and irradiation creep behavior of fcc-austenitic and bcc-ferritic/martensitic alloys at high neutron exposure, *Journal of Nuclear Materials* **276**, 123 (2000).
- [37] A. P. Thompson, H. M. Aktulga, R. Berger, D. S. Bolinteanu, W. M. Brown, P. S. Crozier, P. J. in 't Veld, A. Kohlmeyer, S. G. Moore, T. D. Nguyen, R. Shan, M. J. Stevens, J. Tranchida, C. Trott, and S. J. Plimpton, LAMMPS - a flexible simulation tool for particle-based materials modeling at the atomic, meso, and continuum scales, *Computer Physics Communications* **271**, 108171 (2022).
- [38] P. Hirel, AtomsK: A tool for manipulating and converting atomic data files, *Computer Physics Communications* **197**, 212 (2015).
- [39] G. J. Ackland, M. I. Mendeleev, D. J. Srolovitz, S. Han, and A. V. Barashev, Development of an interatomic potential for phosphorus impurities in α -iron, *Journal of Physics: Condensed Matter* **16**, S2629 (2004).
- [40] J. Hao, L. Casillas-Trujillo, and H. Xu, Using lifetime of point defects for dislocation bias in bcc fe, *Current Opinion in Solid State and Materials Science* **26**, 10.1016/j.cossms.2022.101021 (2022), cited by: 0.

- [41] X. Li, C. Ding, Y. Zhang, Y. Xu, X. Li, X. Wang, Q. Fang, X. Wu, and C. Liu, Vacancy accumulation mechanism at iron grain boundaries: The influence of grain boundary character and its coupling with grain size, *Journal of Nuclear Materials* **579**, 10.1016/j.jnucmat.2023.154386 (2023), cited by: 0.
- [42] D. Terentyev, K. Vörtler, C. Björkas, K. Nordlund, and L. Malerba, Primary radiation damage in bcc fe and fe-cr crystals containing dislocation loops, *Journal of Nuclear Materials* **417**, 1063 – 1066 (2011), cited by: 25.
- [43] Y. Li, S. Hu, C. H. Henager Jr., H. Deng, F. Gao, X. Sun, and M. A. Khaleel, Computer simulations of interstitial loop growth kinetics in irradiated bcc fe, *Journal of Nuclear Materials* **427**, 259 – 267 (2012), cited by: 25.
- [44] D. J. Hepburn and G. J. Ackland, Metallic-covalent interatomic potential for carbon in iron, *Phys. Rev. B* **78**, 165115 (2008).
- [45] J. ye Li, H. cai Xie, W. qing Meng, X. ming Zhang, W. hong Zhao, and G. feng Shi, Evolution mechanism of subsurface defect structure in particle micro-cutting iron-carbon alloy process, *Proceedings of the Institution of Mechanical Engineers, Part J: Journal of Engineering Tribology* **235**, 931 (2021), <https://doi.org/10.1177/1350650120928225>.
- [46] D. Terentyev, N. Anento, A. Serra, V. Jansson, H. Khater, and G. Bonny, Interaction of carbon with vacancy and self-interstitial atom clusters in α -iron studied using metallic-covalent interatomic potential, *Journal of Nuclear Materials* **408**, 272 (2011).
- [47] F. Granberg, D. Terentyev, and K. Nordlund, Interaction of dislocations with carbides in bcc fe studied by molecular dynamics, *Journal of Nuclear Materials* **460**, 23 (2015).
- [48] N. Gunkelmann, H. Ledbetter, and H. M. Urbassek, Experimental and atomistic study of the elastic properties of α' Fe-C martensite, *Acta Materialia* **60**, 4901 (2012).
- [49] S. Chandrasekhar, Stochastic problems in physics and astronomy, *Rev. Mod. Phys.* **15**, 1 (1943).
- [50] R. Kubo, The fluctuation-dissipation theorem, *Reports on Progress in Physics* **29**, 255 (1966).
- [51] D. Mason, Incorporating non-adiabatic effects in embedded atom potentials for radiation damage cascade simulations, *Journal of Physics: Condensed Matter* **27**, 145401 (2015).
- [52] A. Stukowski, Visualization and analysis of atomistic simulation data with ovito—the open visualization tool, *Modelling and Simulation in Materials Science and Engineering* **18**, 015012 (2009).
- [53] P. M. Larsen, S. Schmidt, and J. Schiøtz, Robust structural identification via polyhedral template matching, *Modelling and Simulation in Materials Science and Engineering* **24**, 055007 (2016).
- [54] J. S. Dai, Euler-rodriques formula variations, quaternion conjugation and intrinsic connections, *Mechanism and Machine Theory* **92**, 144 (2015).
- [55] A. Albou, J. Driver, and C. Maurice, Microband evolution during large plastic strains of stable 110 \langle 112 \rangle al and al-mn crystals, *Acta Materialia* **58**, 3022 (2010).
- [56] A. Stukowski, V. V. Bulatov, and A. Arsenlis, Automated identification and indexing of dislocations in crystal interfaces, *Modelling and Simulation in Materials Science and Engineering* **20**, 085007 (2012).
- [57] S. Ni, Y. Wang, X. Liao, S. Alhajeri, H. Li, Y. Zhao, E. Lavernia, S. Ringer, T. Langdon, and Y. Zhu, Grain growth and dislocation density evolution in a nanocrystalline ni-fe alloy induced by high-pressure torsion, *Scripta Materialia* **64**, 327 (2011).
- [58] Y. Zhang, G. J. Tucker, and J. R. Trelewicz, Stress-assisted grain growth in nanocrystalline metals: Grain boundary mediated mechanisms and stabilization through alloying, *Acta Materialia* **131**, 39 (2017).
- [59] K. K. Alaneme and E. A. Okotete, Recrystallization mechanisms and microstructure development in emerging metallic materials: A review, *Journal of Science: Advanced Materials and Devices* **4**, 19 (2019).
- [60] G. S. Rohrer, Grain boundary energy anisotropy: a review, *Journal of Materials Science* **46**, 5881 (2011).
- [61] W. W. Mullins, Two-Dimensional Motion of Idealized Grain Boundaries, *Journal of Applied Physics* **27**, 900 (2004), https://pubs.aip.org/aip/jap/article-pdf/27/8/900/7922977/900_1_online.pdf.
- [62] P.-W. Ma, D. R. Mason, S. Van Boxel, and S. L. Dudarev, Athermal evolution of nanocrystalline tungsten driven by irradiation, *Journal of Nuclear Materials* **586**, 154662 (2023).
- [63] C. Castan, F. Montheillet, and A. Perlade, Dynamic recrystallization mechanisms of an Fe-8% Al low density steel under hot rolling conditions, *Scripta Materialia* **68**, 360 (2013).
- [64] Z. Wan, Y. Sun, L. Hu, and H. Yu, Experimental study and numerical simulation of dynamic recrystallization behavior of TiAl-based alloy, *Materials & Design* **122**, 11 (2017).
- [65] G. EBRAHIMI, A. MALDAR, H. MONAJATI, and M. HAGHSHENAS, Hot deformation behavior of az91 magnesium alloy in temperature ranging from 350°C to 425°C, *Transactions of Nonferrous Metals Society of China* **22**, 2066 (2012).
- [66] Y. Zhang, S. Jiang, Y. Liang, and L. Hu, Simulation of dynamic recrystallization of niti shape memory alloy during hot compression deformation based on cellular automaton, *Computational Materials Science* **71**, 124 (2013).
- [67] M. Klimenkov, E. Materna-Morris, and A. Möslang, Characterization of radiation induced defects in eurofer 97 after neutron irradiation, *Journal of Nuclear Materials* **417**, 124 (2011), proceedings of ICFRM-14.
- [68] C. Dethloff, E. Gaganidze, and J. Aktaa, Microstructural defects in eurofer 97 after different neutron irradiation conditions, *Nuclear Materials and Energy* **9**, 471 (2016).
- [69] R. Schäublin, B. Décamps, A. Prokhodtseva, and J. Löffler, On the origin of primary $\frac{1}{2}$ a0 \langle 111 \rangle and a0 \langle 100 \rangle loops in irradiated fe(cr) alloys, *Acta Materialia* **133**, 427 (2017).
- [70] F. Humphreys and M. Hatherly, Chapter 13 - hot deformation and dynamic restoration, in *Recrystallization and Related Annealing Phenomena (Second Edition)*, edited by F. Humphreys and M. Hatherly (Elsevier, Oxford, 2004) second edition ed., pp. 415–V.
- [71] R. Wang and T. Lei, Dynamic recrystallization of ferrite in a low carbon steel during hot rolling in the (f+a) two-phase range, *Scripta Metallurgica et Materialia* **31**, 1193 (1994).
- [72] N. Tsuji, Y. Matsubara, Y. Saito, and T. Maki, Occurrence of dynamic recrystallization in ferritic iron, *Jour-*

- nal of the Japan Institute of Metals **62**, 967 (1998).
- [73] H. McQueen, Dynamic recovery and recrystallization, in *Encyclopedia of Materials: Science and Technology*, edited by K. J. Buschow, R. W. Cahn, M. C. Flemings, B. Ilshner, E. J. Kramer, S. Mahajan, and P. Veyssière (Elsevier, Oxford, 2001) pp. 2375–2381.
- [74] C. Sellars, Modelling of structural evolution during hot working processes. (1986) p. 167 – 187, cited by: 41.
- [75] J. Ziman, *Electrons and Phonons: The Theory of Transport Phenomena in Solids* (Oxford University Press, 2001).
- [76] C. V. Nielsen and P. A. Martins, Chapter 2 - formability*, in *Metal Forming*, edited by C. V. Nielsen and P. A. Martins (Academic Press, 2021) pp. 7–107.
- [77] J. Jiang, F. Jiang, and M. Zhang, Dynamic recrystallization and precipitation in an al–mg–sc alloy: effect of strain rate, *Journal of Materials Research and Technology* **19**, 1444 (2022).
- [78] A. P. Mouritz, 4 - strengthening of metal alloys, in *Introduction to Aerospace Materials* (Woodhead Publishing, 2012) pp. 57–90.
- [79] I. Milošev, V. Levašič, S. Kovač, T. Sillat, S. Virtanen, V.-M. Tiainen, and R. Trebše, 3 - metals for joint replacement, in *Joint Replacement Technology (Third Edition)*, Woodhead Publishing Series in Biomaterials, edited by P. Revell (Woodhead Publishing, 2021) third edition ed., pp. 65–122.
- [80] H. Cleaves and J. Hiegel, Properties of high-purity iron, *Journal of Research of the National Bureau of Standards* **28**, 643 (1942).
- [81] R. Causey, R. Karnesky, and C. San Marchi, 4.16 - tritium barriers and tritium diffusion in fusion reactors, in *Comprehensive Nuclear Materials*, edited by R. J. Konings (Elsevier, Oxford, 2012) pp. 511–549.
- [82] R. W. K. H. H. K. D. H. Bhadeshia, *Steels: Microstructure and Properties*, 3rd ed. (Elsevier, Butterworth-Heinemann, Amsterdam ; Boston, 2006).
- [83] D. Stein, The effect of carbon on the strain-rate sensitivity of iron single crystals, *Acta Metallurgica* **14**, 99 (1966).
- [84] X. L. Shu and C. Y. Wang, The motion of dislocation in iron pinning by carbon interstitials, in *PRICM 6*, Materials Science Forum, Vol. 561 (Trans Tech Publications Ltd, 2007) pp. 1865–1868.
- [85] A. Sutton and R. Balluffi, *Interfaces in Crystalline Materials*, 1st ed., Oxford Classic Texts in the Physical Sciences (Oxford University Press, 2009).
- [86] C. A. Wert, Diffusion coefficient of c in α -iron, *Phys. Rev.* **79**, 601 (1950).
- [87] D. Kandaskalov, L. Huang, J. Emo, and P. Maugis, Carbon diffusion in bcc- and bct-fe: Influence of short-range c–c pair interactions studied from first-principles calculations, *Materials Chemistry and Physics* **286**, 126159 (2022).
- [88] K. Tapasa, A. Barashev, D. Bacon, and Y. Osetsky, Computer simulation of carbon diffusion and vacancy–carbon interaction in α -iron, *Acta Materialia* **55**, 1 (2007).
- [89] C.-C. Fu, E. Meslin, A. Barbu, F. Willaime, and V. Oison, Effect of c on vacancy migration in α -iron, *Solid State Phenomena* **139**, 157 (2008).
- [90] D. E. Jiang and E. A. Carter, Carbon dissolution and diffusion in ferrite and austenite from first principles, *Phys. Rev. B* **67**, 214103 (2003).
- [91] C. Domain, C. S. Becquart, and J. Foct, Ab initio study of foreign interstitial atom (c, n) interactions with intrinsic point defects in α -fe, *Phys. Rev. B* **69**, 144112 (2004).
- [92] J. Snoek, Effect of small quantities of carbon and nitrogen on the elastic and plastic properties of iron, *Physica* **8**, 711 (1941).
- [93] M. A. Meyers and K. K. Chawla, *Mechanical Behavior of Materials*, 2nd ed. (Cambridge University Press, 2008).
- [94] A. ARGON, Chapter 21 - mechanical properties of single-phase crystalline media: Deformation at low temperatures, in *Physical Metallurgy (Fourth Edition)*, edited by R. W. CAHN and P. HAASEN† (North-Holland, Oxford, 1996) fourth edition ed., pp. 1877–1955.
- [95] E. Schmid and W. Boas, *Plasticity of crystals: With special reference to metals* (Citeseer, 1950).
- [96] C. Barrett, G. Ansel, and R. Mehl, Slip, twinning and cleavage in iron and silicon ferrite, *Trans. ASM* **25**, 702 (1937).
- [97] P. M. Anderson, J. P. Hirth, and J. Lothe, *Theory of Dislocations, 3rd Edition* (Cambridge University Press, 2017).
- [98] S. Nemat-Nasser, Experimentally-based micromechanical modeling of metal plasticity with homogenization from micro-to macro-scale properties, in *IUTAM Symposium on Micro- and Macrostructural Aspects of Thermoelasticity*, edited by O. T. Bruhns and E. Stein (Springer Netherlands, Dordrecht, 2002) pp. 101–113.
- [99] D. R. Mason, F. Granberg, M. Boleininger, T. Schwarz-Selinger, K. Nordlund, and S. L. Dudarev, Parameter-free quantitative simulation of high-dose microstructure and hydrogen retention in ion-irradiated tungsten, *Phys. Rev. Mater.* **5**, 095403 (2021).
- [100] N. Mortazavi, M. Esmaily, and M. Halvarsson, The capability of transmission kikuchi diffraction technique for characterizing nano-grained oxide scales formed on a ferral stainless steel, *Materials Letters* **147**, 42 (2015).